UNIVERSITY OF CALGARY

Far-Field Linear Optical Superresolution via Heterodyne Detection in a Higher-Order Local Oscillator Mode

by

Fan Yang

A THESIS

SUBMITTED TO THE FACULTY OF GRADUATE STUDIES

IN PARTIAL FULFILLMENT OF THE REQUIREMENTS FOR THE

DEGREE OF MASTER OF SCIENCE

GRADUATE PROGRAM IN PHYSICS AND ASTRONOMY

CALGARY, ALBERTA

AUGUST, 2016

Abstract

Rayleigh criterion has been the unbreakable rule for direct imaging. In the past few decades, new imaging techniques emerged to circumvent Rayleigh limit by changing the imaging conditions. By analysing the optical field in image plane with quantum optics, one can find quantum Fisher information for estimating the distance between two light sources remains constant, which means one can always estimate this distance with finite error. This discovery makes Rayleigh criterion irrelevant to quantum optimal measurements. Inspired by the theoretical analysis, we propose an experimental implementation to achieve sub-Rayleigh resolution. Using optical heterodyne detection with a local oscillator in TEM_{01}, we can measure the single slit position within 0.0015 and 0.012 of Rayleigh limit for coherent and incoherent light. We can also measure the distance between two slits emitting incoherent light within 0.019 of Rayleigh limit. By engaging more Hermite-Gaussian modes, we can reconstruct the full image.

Acknowledgements

I thank Dr. Alexander Lvovsky for all his support for my master's study. He spent numerous hours in the laboratory teaching us experiment and answering question. Many thanks to Dr. Christoph Simon for his help with theoretical analysis. I also thank my co-workers Arina Tashchlina and Evgeny S. Moiseev for their help with the experiment and helpful discussions.

Table of Contents

List of Figures and Illustrations

List of Symbols, Abbreviations and Nomenclature

Symbol	Definition
TEM	transverse electromagnetic mode
NA	Numerical Aperture
STED	stimulated emission depletion
SNOM	scanning near-field optical microscopy
STORM	stochastic optical reconstruction microscopy
PALM	photon activated localization microscopy
MLE	maximum likelihood estimator
SLD	symmetric logarithmic derivative
POVM	positive-operator valued measure
SPADE	spatial-mode demultiplexing
LO	local oscillator
ECDL	external cavity diode laser
PZT	lead zirconate titanate (piezoelectric ceramic material)
RF	radio frequency
AOM	acousto-optic modulator
AC	alternative current
HGM	Hermite-Gaussian microscopy
SLM	spatial light modulator
OST	optical state tomography
SLIVER	super localization by image inversion interferometry

Chapter 1

Introduction

Since the invention of the first microscope in the 16th century, scientists have been trying to improve the resolution of microscopes. In the early days, scientists thought they could achieve arbitrary resolution by making perfect optics. It was not until the 1870s, when Ernst Abbe[1] and Lord Rayleigh[2] published their research on optical imaging systems, that people realized the fundamental resolution limit due to diffraction. For the next century, Rayleigh criterion became the unbreakable rule for microscope designs. Things changed in the past few decades, when talented pioneers started challenging the diffraction limit. Various successful imaging methods[3, 4, 5, 6, 7, 8] that work below Rayleigh limit have been invented and applied to biology and chemistry research. Such techniques are named super-resolution microscopy, highlighting their ability of sub-Rayleigh resolution. In 2014, the Nobel Prize in Chemistry was awarded to Eric Betzig, Stefan W. Hell and William E. Moerner for their development of super-resolved fluorescence microscopy, acknowledging the importance for super-resolution techniques. We begin with a review of resolution limit of direct imaging system and mostly used super-resolution techniques.

1.1 Resolution limit

1.1.1 Point spread function

Point spread function[9] is the diffraction pattern of a point light source in the image plane of an optical system. We can model a direct imaging system with a circular objective lens with focal length f and diameter D. For a single point light source located on the optical axis of the lens, the diffraction pattern in the image plane is a bright circular disc with series of concentric rings. This

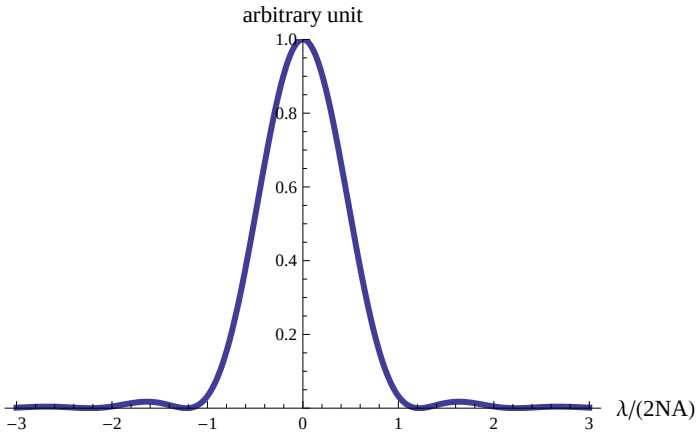

Figure 1.1: Airy pattern

diffraction pattern is called Airy pattern[10]. We normalize Airy pattern in one dimension as

$$I(x) = I_0 \left[\frac{J_1(\pi x)}{\pi x} \right]^2, \tag{1.1}$$

where $J_1(x)$ is the 1st order Bessel function of first kind. The Airy pattern is shown in Figure 1.1. The bright disc in Airy pattern is called Airy disc, whose radius is given by

$$r = 1.22n\frac{f\lambda}{D}, \tag{1.2}$$

where λ is the wavelength of the light in vacuum, while n is the refractive index. An extended object can be thought as comprising of many point light sources, and the image of the object is the sum of the point spread functions from all points of the object.

1.1.2 Rayleigh criterion

Rayleigh criterion has been the convention to determine the resolution limit for direct imaging. It states that two point light sources are just resolvable when the maximum of the Airy disc of one point source coincide with the first minimum of the other. The minimum resolvable distance between the two emitters is

$$d_r = 1.22n\frac{f\lambda}{D}. \tag{1.3}$$

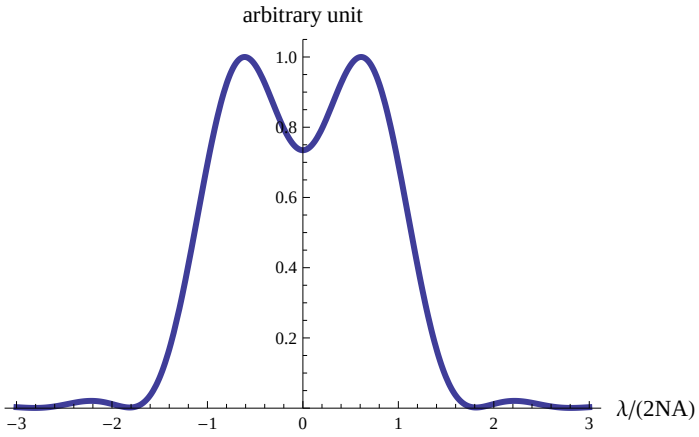

Figure 1.2: Illustration of Rayleigh criterion

This distance is called Rayleigh limit. For microscopes, the objective lens is typically characterized by its numerical aperture (NA) which is defined as

$$NA = nsin\theta, \tag{1.4}$$

where θ is the half angle of the cone of light collection by the objective lens. For $D \ll f$, which is the case of our experiment, the numerical aperture can be approximated by

$$NA = n\frac{D}{2f}. \tag{1.5}$$

We use the expression in equation 1.5 for the rest of the thesis. We can rewrite Rayleigh criterion in term of NA as

$$d_r = 1.22\frac{\lambda}{2NA}. \tag{1.6}$$

This resolution limit is the result of the wave nature of light. In Figure 1.2, we show the intensity distribution in the image plane when two point light sources are separated by Rayleigh limit. The intensity in the centre is approximately 74% of the maximum.

1.1.3 Comparison of various resolution limits

People may use slightly different definitions of resolution limit depending on their field of study. Here we show that all the conventional definitions are equivalent in terms of diffraction. The most

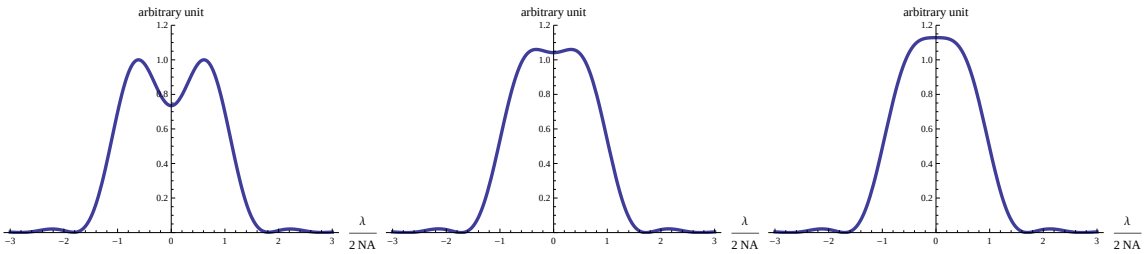

(a) Rayleigh limit $d_r = \frac{1.22\lambda}{2NA}$ (b) Abbe limit $d_r = \frac{\lambda}{2NA}$ (c) Sparrow limit $d_r = \frac{0.94\lambda}{2NA}$

Figure 1.3: Comparison of various conventional resolution limits.

commonly referred conventional resolution limits are: Rayleigh, Abbe and Sparrow criteria, which are compared in Figure 1.3. The difference between those definitions is just the relative intensity at the centre compared to the maximum, which are 74%, 98% and 100%, respectively. Rayleigh and Abbe criteria are mostly used in conventional microscopy, while Sparrow criterion is often used in astronomy. We use Rayleigh criterion as the standard definition.

1.1.4 Gaussian approximation of Airy pattern

Airy pattern is mathematically complicated for calculations. We can approximate Airy pattern by a Gaussian function if we are not concerned with the concentric rings. The optimal approximation with the same central intensity is give by

$$I(x) = I_0 e^{-x^2/2\sigma^2}, \tag{1.7}$$

where $\sigma = 0.21\lambda/NA$[32]. The difference between these two functions is shown in Figure 1.4. The blue curve is the Airy pattern, while the red one is the Gaussian approximation.

1.2 Abbe theory of imaging

In 1867, Ernst Abbe demonstrated the imaging process for an infinite periodic object[9]. This theory can be generalized to objects of any shape. To understand the imaging process, we first discuss Abbe's demonstration in an intuitive way, and then formalize the result as a double Fourier transform.

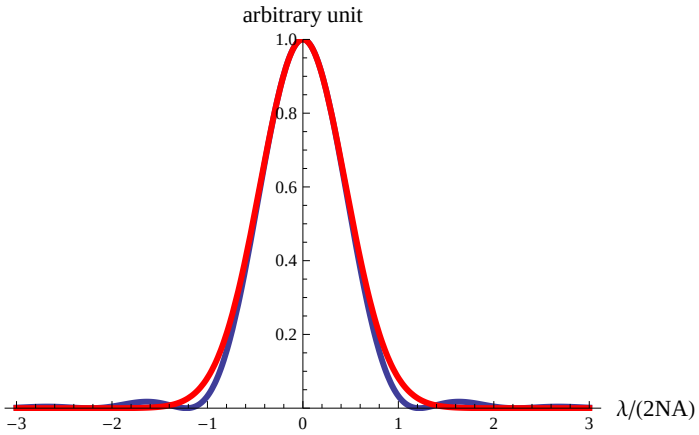

Figure 1.4: Gaussian approximation of Airy pattern. Blue: Airy pattern, Red: Gaussian approximation.

Consider an infinite periodic object located in the object plane. Each diffraction order from this object, in the paraxial approximation, can be treated as a plane wave. After transmitting through the objective lens, the plane waves are focused at different points on focal plane and continue to propagate and overlap again, forming an image in the image plane. There are two stages in the process. On the first stage, Fraunhofer diffraction pattern is formed on the focal plane; on the second stage, the diffraction orders on the Fourier plane behaves like equally spaced point sources and their diffraction pattern is the image. An object of arbitrary shape can be described as the sum of a series of infinite periodic patterns. Thus, the above-mentioned process can be applied to any object.

We can understand the distortion of the image as follows. For an infinite lens, all the diffraction orders are collected by the objective lens. When they interfere and form the image, no information is lost. However, for a lens of finite size, higher orders of diffraction cannot transmit the objective lens. Those diffraction orders contain information of the fine structure of the object. Loss of this information results in a distorted blurry image.

Next, we formalize this process in one dimension with a double Fourier transform. It can be easily extended to two dimensions. Suppose the spatial distribution of the optical field in the object

plane is $E(x)$. The optical field on the focal plane is the Fourier transform of $E(x)$,

$$\tilde{E}(k_\perp) = \int_{-\infty}^{+\infty} E(x) e^{ik_\perp x} dx, \tag{1.8}$$

where $k_\perp$ is the orthogonal component of the wavevector. The change of optical phase and the normalization factor are neglected. In the image plane, the inverse Fourier transform is applied, resulting in the field distribution

$$\begin{aligned} E'(x') &= \int_{-\infty}^{+\infty} \tilde{E}(k_\perp)\tilde{T}(k_\perp) e^{-ik_\perp x'} dk_\perp \\ &= \int_{-\infty}^{+\infty}\int_{-\infty}^{+\infty} E(x)\tilde{T}(k_\perp) e^{ik_\perp (x-x')} dx dk_\perp, \end{aligned}$$

where $\tilde{T}(k_\perp)$ is the transmissivity of the lens. If the transimissivity is constant, we have $E'(x') = E(x)$. This means the image formed by an infinite lens is identical to the object. In reality, a lens with a finite width makes the image distorted according to

$$E'(x') = \int_{-\infty}^{+\infty} E(x) T(x'-x) dx, \tag{1.9}$$

where

$$T(x'-x) = \int_{-\infty}^{+\infty} \tilde{T}(k_\perp) e^{ik_\perp (x-x')} dk_\perp \tag{1.10}$$

is the Fourier image of the lens. In other words, the image is a convolution of the object with $T(x)$. $T(x)$ is called the transfer function of the objective lens.

1.3 Review of super-resolution techniques

Many super-resolution techniques have been used in biology research with great success. Here we present a brief review of these techniques and discuss why new techniques are still needed.

1.3.1 Super-resolution with nonlinear optics

One way to achieve sub-Rayleigh resolution is to take advantage of nonlinearities in optical media. The most successful techniques are two-photon excitation microscopy[3] and stimulated emission

depletion microscopy[4].

Two-photon excitation was first theoretically analysed by Maria Göppert Mayer in 1931[12] and observed in experiments by Kaiser and Garrett in 1961[13]. Denk *et al.*[3] first combined microscopy with two-photon excitation in 1990. In two-photon excitation microscopy, one florescence photon is precedent with a two-photon absorption. This process requires simultaneous absorption of the two photons, therefore has a extremely low probability. To increase the number of excitations, a strong flux of photons is required. In experiments, one can maximize the two-photon excitation efficiency by focusing a powerful laser beam to its diffraction limit, which is typically achieved by focusing a 1W pulsed laser to 10^{-9} cm^2. Two-photon excitation is a non-linear process, whose probability is proportional to the square of optical intensity. For a highly focused beam, the intensity in the vicinity of the focal point decreases quadratically with the distance along the direction of propagation z. As a result, only the small region around the focal point is excited. By scanning the focal point of the laser on the object, we can obtain the image with an increased resolution.

Stimulated emission depletion (STED) microscopy was developed by Stefan W. Hell and Jan Wichmann in 1994[4]. They achieve super-resolution by inhibiting the fluorescence process in the outer region of the excitation point. A pair of synchronized pulsed lasers are used in STED microscopy. Each pair of laser pulses comprises of an excitation pulse and a depletion pulse. The first pulse excite the sample, creating a spot still within the diffraction limit. The depletion pulse (also called STED pulse) is sent immediately after the excitation pulse. The STED pulse is red shifted to the emission spectrum of the sample and clears the excitation by stimulated emission. By manipulating the spatial profile of the STED pulse to a doughnut shape with a zero intensity in the centre, the excitations in the periphery of the spot are depleted while the centre spot remains unaffected. By making the central zero intensity region smaller than the diffraction limit, one can achieve sub-Rayleigh resolution in the transverse plane.

1.3.2 Near-field super-resolution

Rayleigh criterion only applies to far-field imaging and we can circumvent this limit by detection in near-field. Such a technique is called scanning near-field optical microscopy (SNOM)[5, 6]. E. H. Synge first proposed the idea of near field imaging in 1928[14]. But this proposal was soon forgotten due to its technical challenges. In 1984, Pohl *et al.* implemented this method in experiments for the first time. In SNOM, a sub-wavelength aperture is placed in the near-field of an object. This small aperture acts as a light source, whose dimension to a great extend determines the spatial resolution of the microscope. The aperture is usually implemented by a tapered nanofibre with metal coating around the tip. By scanning the aperture on the surface of the object, an image with resolution beyond diffraction limit can be obtained.

1.3.3 Localization microscopy

Another branch of super-resolution techniques is localization microscopy. In localization microscopy, the position of an individual point source can be measured with high precision, which is not restricted by diffraction limit. One can isolate fluorophores located within diffraction limit from each other by turning on only a fraction of photo-switchable fluorophores. The position of those fluorophores are measured in one imaging cycle. By repeating the imaging cycles with different fluorophores, one can reconstruct the image with a resolution higher than direct imaging. Such techniques include stochastic optical reconstruction microscopy (STORM)[7], photon activated localization microscopy (PALM)[8], etc.

1.3.4 Discussion

All these aforementioned super-resolution techniques have found successful applications in biophysics. While two-photon excitation microscopy typically achieves a resolution two to three times better than direct imaging, all the other techniques can achieve a resolution of $\sim$ 20 nm, about ten times better than Rayleigh limit. However, they do not violate Rayleigh criterion, but

rather circumvent the diffraction limit by changing the imaging conditions. Rayleigh criterion holds on two conditions: far-field detection and simultaneous emitting of light sources. None of these techniques can achieve sub-Rayleigh resolution without violating one of the two conditions. These techniques also suffer from high cost and difficulty of operation due to their complicated methodology. Two-photon excitation microscopy and STED microscopy requires sub-picosecond laser pulses; SNOM works only for the surface of an object; STORM and PALM can be used only if the object is photo-switchable. In many cases, imaging in far-field is required and simple operation is expected. In this thesis, we demonstrate a new technique to achieve super-resolution with linear optics in far-field. Inspired by the theoretical proposal by Tsang *et al.*[15], we achieve sub-Rayleigh resolution without breaking either of the two conditions for Rayleigh criterion to hold. The theoretical analysis by Tsang *et al.* and our experimental result fundamentally change the understanding of diffraction limit.

Chapter 2

Theory

In direct imaging system, the indistinguishability of two point sources within Rayleigh limit comes from the unlimited estimation error of their separation distance. In statistics, the precision to estimate an unknown parameter θ from an observable random variable X is described by Cramér-Rao bound, which can be calculated from Fisher information. Tsang *et al.*[15] find that Fisher information does not vanish for estimating separation distance of two light sources even they are closer than the Rayleigh limit if we describe the imaging process quantum mechanically. By counting photon numbers in each Hermite-Gaussian mode, one can acquire classical Fisher information equal to its quantum counterpart. Therefore, the resolution is only limited by quantum noise, making Rayleigh criterion irrelevant to the problem. Inspired by their analysis, we implement the detection in a different fashion. We measure field amplitudes of the image in higher Hermite-Gaussian modes by optical heterodyne detection, circumventing the technical challenge to count photon numbers in different transverse electromagnetic modes (TEMs).

2.1 Parameter estimation in statistics

Before introducing quantum description of the imaging process, it is useful to understand classical Fisher information and Cramér-Rao bound in statistics[16].

2.1.1 Fisher information

In parameter estimation problems, we obtain information about an unknown parameter θ from an observable random variable X, whose distribution depends on θ. Consider a probability density

function $f(x|\theta)$. Fisher information is defined as

$$\begin{aligned} I(\theta) &= E_\theta \left[\left(\frac{\partial}{\partial \theta} \log f(x|\theta) \right)^2 \right] \\ &= \int_{-\infty}^{+\infty} \left[\frac{\partial}{\partial \theta} \log f(x|\theta) \right]^2 f(x|\theta)\, dx, \end{aligned} \tag{2.1}$$

where $E_\theta[\cdot]$ represents the expectation of X with parameter θ. We can define the likelihood function to estimate θ. The likelihood to obtain a given outcome of x with varying θ is

$$L(\theta|x) = f(x|\theta). \tag{2.2}$$

Different from $f(x|\theta)$, the likelihood function is a function of θ with parameter x, and therefore it is not a probability distribution. The partial derivative of log-likelihood function with respect to θ

$$S = \frac{\partial}{\partial \theta} \log L(\theta|x) \tag{2.3}$$

is called score in statistics. It is easy to find that the expectation value of score is zero,

$$\begin{aligned} E_\theta \left[\frac{\partial}{\partial \theta} \log f(x|\theta) \right] &= \int_{-\infty}^{+\infty} \left[\frac{\partial}{\partial \theta} \log f(x|\theta) \right] f(x|\theta)\, dx \\ &= \int_{-\infty}^{+\infty} \frac{\frac{\partial}{\partial \theta} f(x|\theta)}{f(x|\theta)} f(x|\theta)\, dx \\ &= \int_{-\infty}^{+\infty} \frac{\partial}{\partial \theta} f(x|\theta)\, dx = 0. \end{aligned} \tag{2.4}$$

Therefore, Fisher information is the variance of the score. In most experiments, $f(x|\theta)$ is twice differentiable. In this case, we can write Fisher information in terms of the second derivative of the log-likelihood function. Notice that

$$\frac{\partial^2}{\partial \theta^2} \log f(x|\theta) = \frac{\frac{\partial^2}{\partial \theta^2} f(x|\theta)}{f(x|\theta)} - \left(\frac{\partial}{\partial \theta} \log f(x|\theta) \right)^2 \tag{2.5}$$

and

$$E_\theta \left[\frac{\frac{\partial^2}{\partial \theta^2} f(x|\theta)}{f(x|\theta)} \right] = \int_{-\infty}^{+\infty} \frac{\partial^2}{\partial \theta^2} f(x|\theta)\, dx = \frac{\partial^2}{\partial \theta^2} \int_{-\infty}^{+\infty} f(x|\theta)\, dx = \frac{\partial^2}{\partial \theta^2} 1 = 0. \tag{2.6}$$

We can write Fisher information as

$$I(\theta) = -E_\theta \left[\frac{\partial^2}{\partial \theta^2} \log f(x|\theta) \right]. \tag{2.7}$$

Fisher information tells us the precision of a maximum likelihood estimator (MLE). We can intuitively understand this as follows. For an MLE, the likelihood function reaches its maximum and the score vanishes. The precision of MLE depends on the curvature of the log-likelihood function around its extremum. For a big curvature a slightly different estimator corresponds to a much lower likelihood, while for a small curvature the likelihood is almost the same. Larger Fisher information means a lager curvature, therefore a better precision of MLE.

We can also extend the definition of Fisher information for N unknown parameters θ_i, $i = 1,2,...N$. In this case, Fisher information takes the form of an $N \times N$ matrix. The elements of the matrix are defined as the covariance of the score

$$I(\theta)_{ij} = E_\theta \left[\left(\frac{\partial}{\partial \theta_i} \log f(x|\theta) \right) \left(\frac{\partial}{\partial \theta_j} \log f(x|\theta) \right) \right] \tag{2.8}$$

If the matrix is diagonal, each diagonal element $I(\theta)_{i,i}$ represents the Fisher information of the corresponding parameter θ_i and each parameter can be estimated independently. If the off diagonal element $I(\theta)_{i,j}$ is does not vanish, the corresponding parameters θ_i and θ_j are not independent.

2.1.2 Cramér-Rao bound

We introduce Cramér-Rao bound to calculate the variance of an unbiased MLE. An estimator is unbiased if its expectation value is the true value of the parameter. Cramér-Rao bound is defined as the lower bound of the variance of any unbiased estimator $\hat{\theta}$, which is the reciprocal of Fisher information:

$$Var(\hat{\theta}) \geq \frac{1}{I(\theta)}. \tag{2.9}$$

We prove this relation as follows. The covariance of estimator $\hat{\theta}$ and the score is

$$\begin{aligned} Cov_\theta \left[\hat{\theta}, \frac{\partial}{\partial \theta} \log f(x|\theta) \right] &= E_\theta \left[(\hat{\theta} - E_\theta(\hat{\theta})) \left(\frac{\partial}{\partial \theta} \log f(x|\theta) - E_\theta \left[\frac{\partial}{\partial \theta} \log f(x|\theta) \right] \right) \right] \\ &= E_\theta \left[(\hat{\theta} - \theta) \frac{\partial}{\partial \theta} \log f(x|\theta) \right] \\ &= \int_{-\infty}^{\infty} \hat{\theta} \frac{\partial}{\partial \theta} f(x|\theta)\, dx \\ &= \frac{\partial}{\partial \theta} E_\theta(\hat{\theta}) = 1. \end{aligned} \tag{2.10}$$

Here we used the fact that the expectation of score is zero and the expectation of an unbiased estimator is the parameter itself. From Cauchy-Schwartz inequality, we have

$$\left(Cov_\theta\left[\hat{\theta}, \frac{\partial}{\partial\theta}\log f(x|\theta)\right]\right)^2 \leq Var(\hat{\theta})Var\left(\frac{\partial}{\partial\theta}\log f(x|\theta)\right) = Var(\hat{\theta})I(\theta). \tag{2.11}$$

Comparing equation 2.10 and 2.11, we obtain the Cramér-Rao bound in equation 2.9. By using Cramér-Rao bound, we can describe the estimation precision in terms of its variance, which is the same as the standard way one describes experimental error.

2.2 Quantum parameter estimation

We can extend the concept of Fisher information to quantum metrology, and use quantum Cramér-Rao bound to calculate estimation precision. Quantum Fisher information[17] is defined as

$$I^{(Q)}(\rho) = tr[L(\rho)^2\rho], \tag{2.12}$$

where ρ is the density matrix of the quantum state while $L(\rho)$ is the symmetric logarithmic derivative (SLD). The SLD is defined by the following equation

$$\frac{\partial}{\partial\theta}\rho = \frac{1}{2}(\rho L + L\rho) \tag{2.13}$$

In the eigenbasis of ρ, where

$$\rho = \sum_i p_i |e_i\rangle\langle e_i|, \tag{2.14}$$

we can derive SLD as follows. From equation 2.13, we have

$$\left\langle e_i\middle|\frac{\partial}{\partial\theta}\rho\middle|e_j\right\rangle = \left\langle e_i\middle|\frac{1}{2}(\rho L + L\rho)\middle|e_j\right\rangle. \tag{2.15}$$

Replacing ρ with equaiton 2.14 on the right hand side of equation 2.15, we have

$$\begin{aligned}
\left\langle e_i\middle|\frac{\partial}{\partial\theta}\rho\middle|e_j\right\rangle &= \left\langle e_i\middle|\frac{1}{2}\left(\sum_k p_k|e_k\rangle\langle e_k|L + L\sum_k p_k|e_k\rangle\langle e_k|\right)\middle|e_j\right\rangle \\
&= \frac{1}{2}\left(\sum_k p_k\langle e_i|e_k\rangle\langle e_k|L|e_j\rangle + \sum_k p_k\langle e_i|L|e_k\rangle\langle e_k|e_j\rangle\right) \\
&= \frac{1}{2}(p_i\langle e_i|L|e_j\rangle + p_j\langle e_i|L|e_j\rangle) \\
&= \frac{p_i+p_j}{2}\langle e_i|L|e_j\rangle.
\end{aligned} \tag{2.16}$$

Therefore, the matrix element of L in the basis of the eigenstates of ρ is

$$\langle e_i|L|e_j\rangle = \frac{2}{p_i+p_j}\left\langle e_i\left|\frac{\partial}{\partial\theta}\rho\right|e_j\right\rangle. \tag{2.17}$$

The complete form of the SLD is

$$L(\rho) = \sum_{i,j}\frac{2}{p_i+p_j}\langle e_i|\frac{\partial\rho}{\partial\theta}|e_j\rangle|e_i\rangle\langle e_j|. \tag{2.18}$$

Quantum Cramér-Rao bound takes the same form as its classical counterpart in equation 2.9, with $I(\theta)$ replaced by $I^{(Q)}(\rho)$.

2.3 Quantum theory of super-resolution

We analyse the imaging process with quantum optics theory following the theoretical proposal by Tsang *et al.*[15]. We show that Fisher information remains constant for estimating the separation distance of two simultaneously emitting incoherent light sources regardless of their separation distance. This allows us to estimate the separation distance with finite error even the light sources are located within Rayleigh limit. For simplicity, we show all calculations in one-dimension. One can easily extend it to two dimensions.

2.3.1 Quantum description of weak thermal sources

We describe the light in the image plane with quantum optics by assuming quasi-monochromatic paraxial light with one polarization. The incoherent light in the image plane can be described by a multimode thermal state with density matrix ρ. We can write ρ in the multimode Fock basis. Let us denote n-photon multimode Fock state as $|n\rangle = |n_1\rangle|n_2\rangle...|n_J\rangle$, where n_j is the photon number in the jth mode and $n = \sum_j n_j$ is the total photon number. Due to the random phase correlation of incoherent light, ρ is diagonal in the multimode Fock basis (see Appendix A)

$$\rho = \sum_{n=0}^{\infty}\pi_n\rho_n,. \tag{2.19}$$

where ρ_n is the density matrix of the multimode n-photon Fock state, while π_n is the corresponding probability. Within the short coherence time of thermal state, we assume the average photon number ε in the image plane is much smaller than one. In this case, ρ can be approximated to the leading order of ε as follows (see Appendix A)

$$\rho = (1-\varepsilon)\rho_0 + \varepsilon\rho_1. \tag{2.20}$$

The vacuum state ρ_0 does not contain any information, so we focus on ρ_1. Assume we have two light sources at position $x = x_q$, $q = 1,2$. The multimode single photon Fock state of light source x_q is

$$|\psi_q\rangle = \sum_j \psi_{j,x_q} |1_j\rangle, \tag{2.21}$$

where $|1_j\rangle$ is the single photon Fock state in the jth mode and ψ_{j,x_q} is the wavefunction. We can also write the single photon state $|\psi_q\rangle$ in the position basis as

$$|\psi_q\rangle = \int_{-\infty}^{\infty} dx \psi_q(x) |x\rangle. \tag{2.22}$$

Because the light is incoherent, we can write ρ_1 as the mixture state of $|\psi_1\rangle$ and $|\psi_2\rangle$ (see Appendix A)

$$\rho_1 = \frac{1}{2}(|\psi_1\rangle\langle\psi_1| + |\psi_2\rangle\langle\psi_2|) \tag{2.23}$$

Notice that the two single photon states are not orthogonal

$$\langle\psi_1|\psi_2\rangle \neq 0. \tag{2.24}$$

This gives us the fundamental difficulty to discern the two states.

2.3.2 Image plane photon counting

To reconstruct the density matrix in the image plane, we can count photon numbers n_i each pixel. With the assumption of $\varepsilon \ll 1$, the photon statistics follows Poissoin distribution. In a photon counting time interval that is the same as the coherence time, the photon number distribution is

$$P(n_1, n_2, ..., n_N) = \prod_i e^{-\varepsilon\Lambda_i} \frac{(\varepsilon\Lambda_i)^{n_i}}{n_i!}, \tag{2.25}$$

where $\varepsilon\Lambda_i$ is the average photon number in the ith pixel while

$$\Lambda_i = \frac{1}{2}(|\psi_{i,x_1}|^2 + |\psi_{i,x_2}|^2) \tag{2.26}$$

is the probability of detecting a photon in the ith pixel. For a time interval m times of the coherence time, the photon statistics is still approximately Poissonian,

$$P^{(m)}(n_1, n_2, ..., n_k) = \prod_i e^{-N\Lambda_i} \frac{(N\Lambda_i)^{n_i}}{n_i!}, \tag{2.27}$$

where $N = m\varepsilon$ is the average number of photons arriving in the image plane during this time interval. By reconstructing the photon number distribution in each pixel, we can estimate the probability of a photon detected in the ith pixel and the position of each light source.

2.3.3 Estimation of separation distance

We can analyse the estimation error of separation distance from quantum Cramér-Rao bound. The density matrix ρ in the image plane depends on two unknown parameters: the centroid θ_1 and separation distance of the two sources θ_2 in the image plane. For image plane photon counting, we use photon numbers to estimate Λ_i, and then use Λ_i to estimate θ_1 and θ_2. Since we can estimate Λ_i with arbitrary precision with sufficiently many counting intervals, we can treat Λ_i as the observable random variable when estimating θ_1 and θ_2. The classical Fisher information is therefore

$$\begin{aligned} I_{\mu\nu} &= E\left[\left(\frac{\partial}{\partial\theta_\mu}\log\Lambda_i\right)\left(\frac{\partial}{\partial\theta_\nu}\log\Lambda_i\right)\right] \\ &= \sum_i \frac{1}{\Lambda_i}\frac{\partial\Lambda_i}{\partial\theta_\mu}\frac{\partial\Lambda_i}{\partial\theta_\nu}, \mu,\nu = 1,2. \end{aligned} \tag{2.28}$$

In the continuous limit, one can count photon numbers at each position in the image plane. The single photon Fisher information becomes

$$I_{\mu\nu} = \int_{-\infty}^{\infty} \frac{1}{\Lambda(x)}\frac{\partial\Lambda(x)}{\partial\theta_\mu}\frac{\partial\Lambda(x)}{\partial\theta_\nu}\,dx, \tag{2.29}$$

where

$$\Lambda(x) = \frac{1}{2}[|\psi_1(x)|^2 + |\psi_2(x)|^2] \tag{2.30}$$

is the probability of detecting a photon at position x. We can calculate the Fisher information for direct imaging. For simplicity, we assume a Gaussian transfer function

$$T(x) = \frac{1}{(2\pi\sigma^2)^{1/4}} e^{-x^2/4\sigma^2} \tag{2.31}$$

with $\sigma = 0.21\lambda/NA$. In most cases, this is a good approximation for the typical Airy pattern of an imaging system.

For two light sources at positions $x = x_1$ and $x = x_2$, we assume the imaging system is spatially invariant, and the wavefunction of a light source at $x = 0$ is $\psi(x)$. We have $\psi_\beta = \psi(x - x_\beta)$. The wavefunction $\psi(x)$ with a Gaussian transfer function becomes

$$\psi(x) = \frac{1}{(2\pi\sigma^2)^{1/4}} e^{-x^2/4\sigma^2}. \tag{2.32}$$

To estimate θ_2, we calculate the Fisher information as follows.

$$\frac{\partial\Lambda(x)}{\partial\theta_2} = \frac{1}{2\sqrt{2\pi}\sigma^3}\left[(x-\theta_1-\frac{\theta_2}{2})e^{-(x-\theta_1-\frac{\theta_2}{2})^2/2\sigma^2} - (x-\theta_1+\frac{\theta_2}{2})e^{-(x-\theta_1+\frac{\theta_2}{2})^2/2\sigma^2}\right] \tag{2.33}$$

vanishes at $\theta_2 = 0$, while $\Lambda(x)$ remains nonzero, resulting in a zero classical Fisher information at $\theta_2 = 0$. The classical Fisher information is

$$I_{22} = \int_{-\infty}^{+\infty} \frac{e^{-\theta_2(x-\theta_1)/\sigma^2}}{8\sigma^5\sqrt{2\pi}} \frac{[\theta_2 + 2(x-\theta_1) + \theta_2 e^{\theta_2(x-\theta_1)/\sigma^2} - 2(x-\theta_1)e^{\theta_2(x-\theta_1)/\sigma^2}]^2}{e^{(x-\theta_1-\theta_2/2)^2/2\sigma^2} + e^{(x-\theta_1+\theta_2/2)^2/2\sigma^2}} dx, \tag{2.34}$$

which can be calculated numerically. This classical Fisher information is just associated with direct imaging. There is no restriction to increasing it by changing the detection method.

The best performance of all possible quantum measurements is quantified by quantum Fisher information. If we choose centroid θ_1 and separation θ_2 as unknown parameters, quantum Fisher information matrix is diagonal. The diagonal elements of single photon quantum Fisher information are (see Ref. [15] for derivation)

$$I_{11}^{(Q)} = 4(\Delta k^2 - \gamma^2), \tag{2.35}$$

$$I_{22}^{(Q)} = \Delta k^2, \tag{2.36}$$

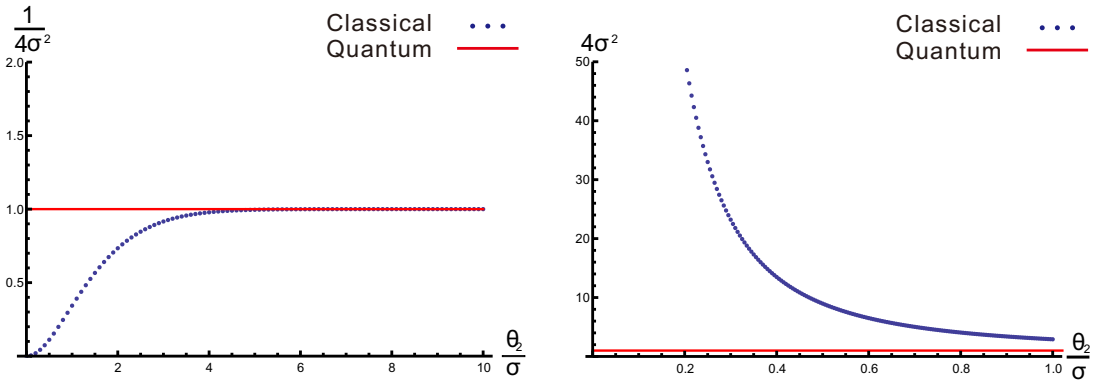

(a) Quantum vs classical Fisher information (b) Quantum vs classical Cramér-Rao bound

Figure 2.1: Comparison of quantum optimal measurement and direct imaging. a)Fisher information b) Cramér-Rao bound

where

$$\Delta k^2 = \int_{-\infty}^{\infty} dx \left[\frac{\partial \psi(x)}{\partial x}\right]^2, \tag{2.37}$$

$$\gamma = \int_{-\infty}^{\infty} dx \frac{\partial \psi(x)}{\partial x} \psi(x-\theta_2). \tag{2.38}$$

Δk^2 is the spatial-frequency invariance of point spread function. When $\theta_2 \to \infty$, $\gamma^2 \to 0$ and $I_{11}^{(Q)} = 4\Delta k^2$ is the standard shot noise limit for localization estimation of single source (see section 4.3 for discussion).

Assuming the same Gaussian transfer function expressed in equation 2.31, $I_{22}^{(Q)}$ becomes

$$I_{22}^{(Q)} = \frac{1}{4\sigma^2} \tag{2.39}$$

As we can see from equation 2.39, the quantum Fisher information for separation distance estimation remains constant, which means the estimation error remains constant and finite regardless of the distance. This is a surprising result, because it proves that Rayleigh limit does not exist for optimal quantum measurement.

To compare quantum optimal measurement and direct imaging, we plot the quantum and classical Fisher information and their corresponding Cramér-Rao bounds in Figure 2.1. Without loss of generality, we assume $\theta_1 = 0$. As we can see, classical Cramér-Rao bound goes to infinity for $\theta_2 \to 0$, while quantum Cramér-Rao bound remains constant.

2.3.4 Spatial-mode demultiplexing

We have proven that for quantum optimal measurements, quantum Cramér-Rao bound for separation distance estimation is constant. However, direct imaging cannot achieve the quantum Cramér-Rao bound. In this section, we introduce a measurement proposed by Tsang *et al.*[15], which could reach the quantum limit.

Instead of counting photons at different positions in the image plane, Tsang *et al.* proposed to count photons in discrete Hermite-Gaussian modes. The Hermite-Gaussian modes $|\psi_n(x)\rangle$, in the position basis, can be expressed as

$$|\phi_n(x)\rangle = \int_{-\infty}^{\infty} \phi_n(x) |x\rangle \, dx, \tag{2.40}$$

$$\phi_n(x) = \frac{1}{(2\pi\sigma^2)^{1/4}\sqrt{2^n n!}} H_n\left(\frac{x}{\sqrt{2}\sigma}\right) exp\left(-\frac{x^2}{4\sigma^2}\right), \tag{2.41}$$

where

$$H_n(x) = (-1)^n e^{x^2} \frac{d^n}{dx^n} e^{-x^2} \tag{2.42}$$

are the Hermite polynomials. All the Hermite-Gaussian modes, together with vacuum state $|vac\rangle$, constitute the following positive-operator valued measure (POVM),

$$E_0 = |vac\rangle \langle vac|, E_i = |\phi_i\rangle \langle \phi_i|, i = 0, 1, 2, ... \tag{2.43}$$

For a single detection event, the probability of detecting photons in qth mode is

$$P(q) = \frac{1}{2}(|\langle \phi_q|\psi_1\rangle|^2 + |\langle \phi_q|\psi_2\rangle|^2) \tag{2.44}$$

Since the centroid θ_1 can be measured with high precison by direct imaging, we assume it is known for separation estimation and set $\theta_1 = 0$. For a Gaussian transfer function, equation 2.44 becomes

$$P(q) = e^{-Q}\frac{Q^q}{q!}, Q = \frac{\theta_2^2}{16\sigma^2}, \tag{2.45}$$

which is a Poisson distribution with parameter Q. The classical Fisher information for detection of N photons is

$$I_{22}^{(HG)} = N\sum_{q=0}^{\infty} P(q)\left[\frac{\partial}{\partial\theta_2}\log P(q)\right]^2 = \frac{N}{4\sigma^2}, \tag{2.46}$$

which is the same as quantum Fisher information. Therefore counting photon numbers in each Hermite-Gaussian mode is a quantum optimal measurement. This measurement method is named spatial-mode demultiplexing (SPADE) by Tsang *et al.*. For photon counting in M trials, we detect n_q photons in the qth Hermite-Gaussian mode. The unbiased maximum likelihood estimators for Q and θ_2 are

$$\hat{Q}_{ML} = \frac{1}{M}\sum_q n_q, \hat{\theta}_{2ML} = 4\sigma\sqrt{\hat{Q}_{ML}}, \tag{2.47}$$

Maximum likelihood estimation can asymptotically approach Cramér-Rao bound[20].

2.4 Optical heterodyne detection in TEM_{01}

Spatial-mode demultiplexing is a quantum optimal measurement. With maximum likelihood estimation, we can asymptotically approach quantum Cramér-Rao bound. Tsang *et al.* proposed to use a multimode waveguide to separate the Hermite-Gaussian modes. However, this is technically challenging due to the sophistication of the setup. It also suffers from lossy waveguides and dark counts of single photon counting modules.

Here we propose an alternative way to detect image plane optical field in different TEMs. Instead of counting photon numbers, we measure the optical field amplitude associated with each Hermite-Gaussian mode via optical heterodyne detection[21]. Our technique cannot obtain photon number distribution, so we use a different way to estimate the separation distance.

2.4.1 Optical heterodyne detection

The schematic for balanced heterodyne detection is shown in Figure 2.2. A local oscillator (LO) beam and a signal beam with frequency difference Ω interfere on a 50:50 beamsplitter. The output beams from the beamsplitter are incident on the two photodiodes of the heterodyne detector. The photocurrents generated by the two photodiodes are subtracted by an electronic circuit and amplified before being sent to detector output. The detector output is proportional to the multiplication of signal and LO amplitudes[22]. Heterodyne detection is sensitive only to the spatial mode of

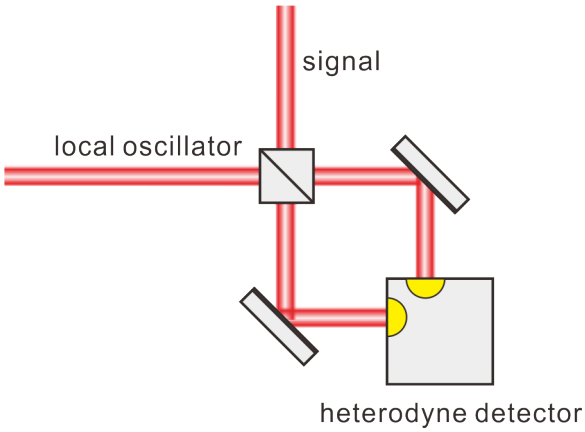

Figure 2.2: Schematic of balanced optical heterodyne detection

the LO[22]. Depending on the electronic noise of the heterodyne detector, this measurement is sensitive up to single photon level[23].

2.4.2 Heterodyne detection in TEM_{01}

From equation 2.45, we know that the probability of a photon being in a Hermite-Gaussian mode decreases dramatically as the mode order increases. So we focus on the first nontrivial mode TEM_{01} and calculate the heterodyne output for a LO in this mode. Quantum description of light is not needed. We treat the light field as a classical electromagnetic wave and use a Gaussian transfer function to approximate Airy pattern (cf. section 1.4)

$$T(x) = \frac{1}{(2\pi\sigma^2)^{1/4}} e^{-x^2/4\sigma^2}, \tag{2.48}$$

where $\sigma = 0.21\lambda/NA$.

Consider a field amplitude distribution $E(x)$ in the object plane. in the image plane, the field is the convolution of $E(x)$ and transfer function $T(x)$

$$E'(x') = \int_{-\infty}^{\infty} E(x)T(x'-x)\,dx. \tag{2.49}$$

The heterodyne detector generates a current that is proportional to the overlap between LO and signal fields

$$J = \int_{-\infty}^{\infty} E'(x')E_{LO}(x')\,dx', \tag{2.50}$$

where $E_{LO}(x')$ is the spatial profile of the LO on image plane. Suppose the LO is aligned such that the corresponding TEM_{00} is matched to the image of a point source located at $x = 0$, the LO profile in TEM_{01} becomes

$$E_{LO}(x') = \frac{1}{(2\pi)^{1/4}\sigma^{3/2}} x' e^{-x'^2/4\sigma^2}. \tag{2.51}$$

Consider a pointed source located at position x_p with $E(x) = \delta(x - x_p)$. In this case, heterodyne current becomes

$$J(x_p) = \int_{-\infty}^{\infty} T(x' - x_p) E_{LO}(x')\, dx'. \tag{2.52}$$

For a Gaussian transfer function, it reduces to a simple expression

$$J(x_p) = \frac{1}{2\sigma} x_p e^{-x_p^2/8\sigma^2}. \tag{2.53}$$

The corresponding electronic output power is

$$P(x_p) \propto J^2(x_p) = \frac{1}{4\sigma^2} x_p^2 e^{-x_p^2/4\sigma^2}, \tag{2.54}$$

which vanishes at x_p. This zero output enables sensitive null measurement of the position of a single source. This result is also extremely useful for estimating the distance d between two incoherent light sources. Suppose the sources are located at $x = \pm d/2$. For two incoherent light sources, the output signal power is $P(d/2) + P(-d/2)$, which is proportional to d^2 to the leading order. The intensity of direct imaging is given by

$$I(x') = S(x' + d/2) + S(x' - d/2) \tag{2.55}$$

where $S(x) = |T(x)|^2$ is the point spread function of the imaging system. If we approximate $S(x' \pm d/2)$ with the Taylor expansion

$$S(x' \pm d/2) = S(x') \pm \frac{d}{2} \frac{\partial}{\partial x} S(x') + O(d^2), \tag{2.56}$$

the image plane intensity distribution becomes

$$I(x') = 2S(x') + O(d^2). \tag{2.57}$$

It is also on the order of d^2, but with a macroscopic zeroth-order background. Noise in this background is detrimental to the precision to estimate d.

To calculate the output power of heterodyne detector for incoherent light, we need to take average of all possible realizations of $E(x)$

$$\begin{aligned}\langle P\rangle &= \left\langle \left(\int_{-\infty}^{\infty} E'(x')E_{LO}(x')\,dx \right)^2 \right\rangle \\ &= \int_{-\infty}^{\infty}\int_{-\infty}^{\infty} \langle E'(x')E'(x'')\rangle\, E_{LO}(x')E_{LO}(x'')dx'dx''\end{aligned} \tag{2.58}$$

Using equation 2.49, we have

$$\langle E'(x')E'(x'')\rangle = \int_{-\infty}^{\infty}\int_{-\infty}^{\infty} \langle E(x_1)E(x_2)\rangle\, T(x'-x_1)T(x''-x_2)dx'dx''. \tag{2.59}$$

For fully incoherent light, the spatial correlation function on object plane is a delta function

$$\langle E(x_1)E(x_2)\rangle = I(x_1)\delta(x_1-x_2), \tag{2.60}$$

if we assume equal brightness of two sources. Hence,

$$\langle P\rangle = \int_{-\infty}^{\infty}\int_{-\infty}^{\infty}\int_{-\infty}^{\infty} I(x)T(x'-x_1)T(x''-x_2)E_{LO}(x')E_{LO}(x'')dxdx'dx''. \tag{2.61}$$

If we cover the objective lens with a round diaphragm, under paraxial approximation, the transfer function in Fourier plane is

$$T(k_\perp) = \theta(k_{\perp max} - |k|) \tag{2.62}$$

where $\theta(\cdot)$ is the Heaviside step function with $k_{\perp max} = 2\pi R/(L\lambda)$. In spatial domain, it becomes

$$T(x'-x) = \frac{J_1(k_{\perp\max}(x-x'))}{x-x'} \approx e^{-(x-x')^2/4\sigma^2}, \tag{2.63}$$

where $J_1(\cdot)$ is 1st order Bessel function of first kind. This result is still approximately Gaussian. The signal power for single coherent source is

$$\langle P\rangle = \left(\int_{-\infty}^{\infty} xE(x)e^{-x^2/8\sigma^2}dx \right)^2. \tag{2.64}$$

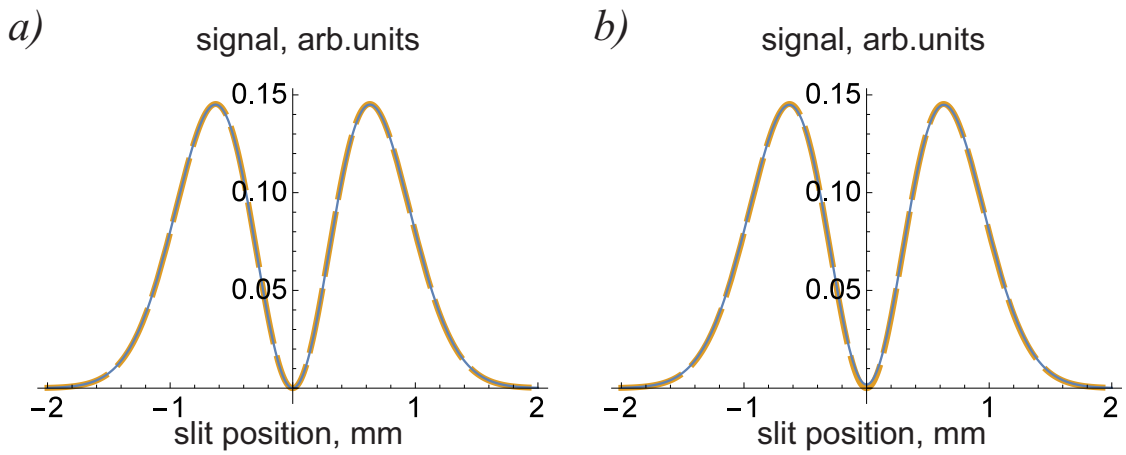

Figure 2.3: Comparison of the theoretical predictions for the signal power of single light source. The only visible difference between the infinitely small slit and finite slit is that the curve for incoherent source with a finite size does not reach zero at $x_p = 0$. a) Coherent case, b) incoherent case.

For incoherent case, the mean signal power is

$$\langle P \rangle = \int_{-\infty}^{\infty} x^2 I(x) e^{-x^2/4\sigma^2}\, dx. \tag{2.65}$$

The result is valid for any distribution of $E(x)$. To illustrate this, we plot output power for a single source with both finite and infinitely small size for coherent and incoherent light in Figure 2.3. The blue thin solid line takes into account the finite size of the light source assuming a diameter of 150μm while the yellow thick dashed line assumes an infinitely small source. The only visible difference between the two models is that the curve for incoherent source with a finite size does not reach zero at $x_p = 0$. This is because an incoherent source with finite size, which can be seen as a combination of multiple mutually incoherent point sources, makes a nonzero contribution to TEM_{01}.

Using equation 2.65, we find the signal power for two incoherent sources separated by d by adding up signals of each source,

$$\begin{aligned} \langle P \rangle &= \left\langle P\left(\frac{d}{2}\right) \right\rangle + \left\langle P\left(-\frac{d}{2}\right) \right\rangle \\ &= 2\int_{-\infty}^{\infty} \left(\frac{d}{2}\right)^2 I\left(\frac{d}{2}\right) e^{-\left(\frac{d}{2}\right)^2/4\sigma^2}. \end{aligned} \tag{2.66}$$

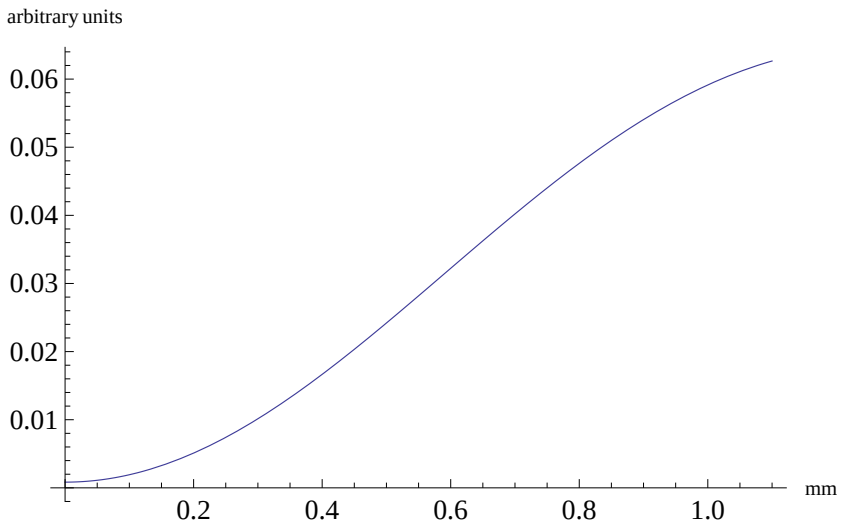

Figure 2.4: Dependence of the signal in TEM_{01} on the separation distance. A finite size of $150\mu m$ is assume for each light source

We plot the signal power of two sources centered at $x = 0$ separated by distance d in Figure 2.4, taking into account of the finite size of the light sources.

2.4.3 Application to super-resolution

Performing optical heterodyne detection in TEM_{01} mode, we can measure position of single source and separation distance of two sources from the output power of heterodyne detector. By fitting the heterodyne power to the theory, we can achieve much higher precision than direct imaging, and also circumvent the technical difficulty associated with photon counting in each Hermite-Gaussian mode.

Chapter 3

Experiment

Hermite-Gaussian modes are orthogonal and optical heterodyne detection is sensitive only to the mode of LO. By preparing LO in TEM_{01}, we can detect the component of signal beam in the same mode. We implement our technique in various settings. First, we measure the position of a single source emitting coherent and incoherent light, respectively. Second, we measure the distance between two incoherent light sources separated below Rayleigh limit.

3.1 Experimental setup

The schematic of the experimental setup is shown in Figure 3.1. We use a home-made external cavity diode laser operating at optical wavelength λ = 780 nm. Both LO and signal beam come from the same laser.

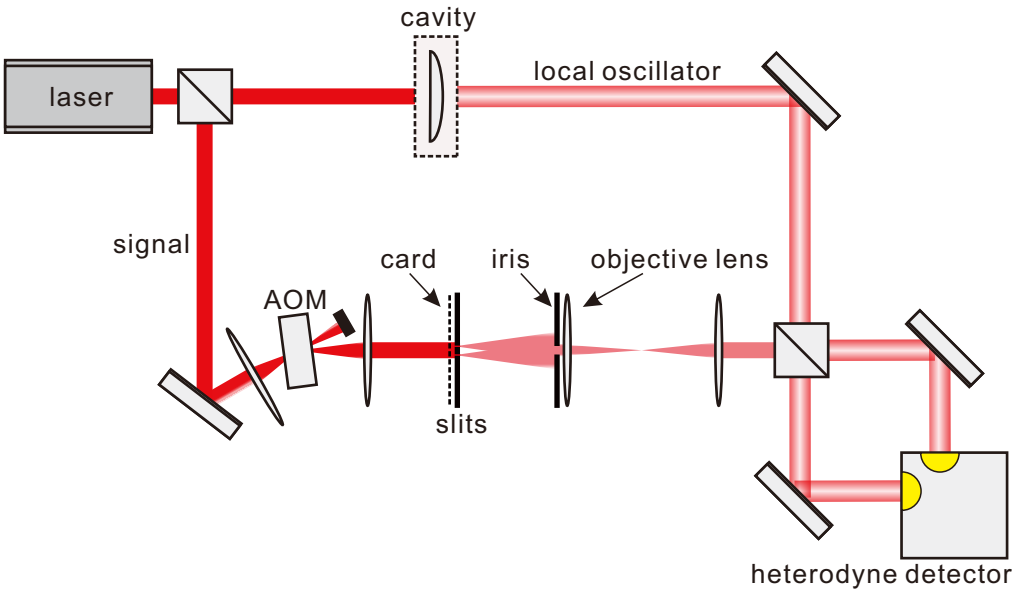

Figure 3.1: Experimental setup

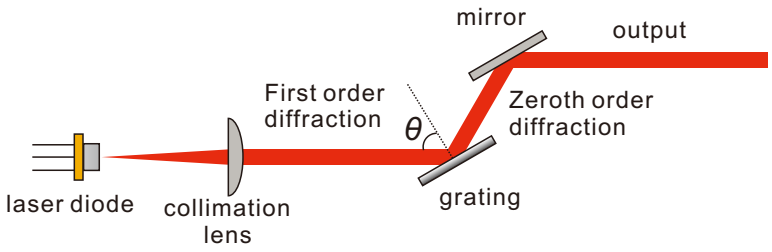

Figure 3.2: Schematic of Littrow configuration external cavity diode laser

3.1.1 External cavity diode laser

External cavity diode laser (ECDL) is commonly used in optics research due to its relatively low price and high performance. ECDL has good tunability and stability, and it is easy to modulate. These features perfectly meet our needs for this experiment. The schematics of an ECDL is shown in Figure 3.2. ECDL makes use of an electrically pumped semiconductor laser, called a diode laser to generate the light beam. We use an aspherical lens to collimate the highly divergent beam emitted by the laser diode. To narrow the linewidth of the laser and select wavelength, a diffraction grating is introduced to give feedback to the laser diode. The first order diffraction is reflected back to the laser diode, while the zeroth order diffraction goes to the output. This design is called Littrow configuration. The wavelength of the reflected beam is determined by the angle of the grating

$$\lambda = \frac{2d}{n} sin\theta, \tag{3.1}$$

where θ is the incident angle of the laser beam. A piezo-electric transducer (PZT) is attached to the grating to change the incident angle and select the desired wavelength. An optional mirror is placed parallel to the grating to redirect the output beam. We can modulate the laser by changing the voltage on the PZT or the current sent to the laser diode. Multiple ways of modulation makes ECDL easy to lock with Pound-Drever-Hall technique (see section 3.1.3). The temperature of the laser diode is maintained by a electronic temperature controller to achieve the maximum stability of laser frequency. A linewidth of tens of kilohertz can be achieve from our home-made ECDL.

3.1.2 Preparation of LO in TEM_{01}

We prepare LO in TEM_{01} by transmitting it through a temperature stabilized monolithic cavity, which was made by P. Palittapongarnpim *et al.*[24] previously in our laboratory. This cavity is made from a BK7 plano-convex lens with high reflectivity coating on both surfaces. The cavity linewidth is $\sim$80 MHz and the finesse is $\sim$275. Its temperature is controlled by a temperature controller (Thorlabs ICT102), which can be fine tuned to 0.1°C. The cavity is put into a thick metal case, which works as a heat sink and isolates the heat transfer between cavity can the environment. Because of Gouy phase shift and its dependence on Hermite-Gaussian modes, different TEMs are resonant with cavity at different frequencies[25]. The frequency f_{mn} of TEM_{mn} is given by $f_{mn} = f_{00} + (m+n)\delta f$, where δf is the frequency difference due to different Gouy phase shift of different TEMs. By adjusting the temperature, we can change the cavity length and therefore change the transmitted mode. We first align the cavity to transmit TEM_{00}. Then we increase the temperature to transmit TEM_{01}. Minor adjustment of optics is required for maximum transmissivity after changing temperature. The transmitted power is maintained at $\sim$ 2.5 mW for all measurements.

3.1.3 Laser lock

We lock the laser frequency to the cavity resonance by Pound-Drever-Hall (PDH) technique[26] to maintain maximum transmission power of LO. We modulate the current sent to the laser diode through a bias tee at f_m =45 MHz, which is still within the linewidth of the cavity. A modulation frequency higher than the linewidth is expected for best performance of PHD lock. However, high frequency modulation also reduces the stability of the laser. A trade-off is made here. We find this modulation frequency works sufficiently for our experiment without introducing extra noise. The modulation of current results in a phase modulation of the laser, generating two sidebands with frequency $f \pm f_m$, where f is the optical frequency without modulation. f is also called the carrier frequency. The sidebands are far from the cavity resonance, and are reflected with no phase shift.

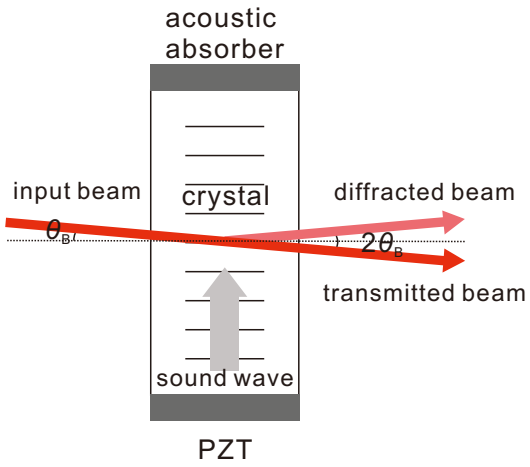

Figure 3.3: Schematic of acousto-optic modulator

On the contrary, the carrier reflected from the cavity acquires a frequency dependent phase. One can use the phase of the sidebands as a reference to detect the phase of the reflected carrier. The interference between the sidebands and the carrier results in an amplitude modulation of the carrier, which can be detected by a photodetector. The output of the photodetector is sent to an electronic circuit. This circuit multiplies the signal from photodetector (RF) with the modulation signal to the laser diode current (electronic local oscillator). If the laser is resonant with the cavity, no carrier is reflected, and the output from the circuit is zero. When the laser is slightly off resonance, the circuit gives an error signal depending on the frequency of the laser. The error signals are opposite when the laser is below and above resonance. In experiments, one needs to adjust the phase between RF and electronic local oscillator to obtain the desired error signal. We amplify this error signal and send it to the PZT in the laser to give a negative feedback to the laser frequency, locking it to the cavity transmission line.

3.1.4 Acousto-optic modulator

To reduce flicker noise in balanced detection, we shift the frequency of the signal beam with an acousto-optical modulator(AOM). An AOM can be used to change the frequency and propagating direction of a laser beam. The schematic of an AOM is shown in Figure 3.3. A PZT is attached to a

transparent crystal. The PZT is driven by an AC electrical voltage (RF signal), generating a sound wave at the same frequency. The sound wave produces a periodical modulation of the refractive index of the crystal. The sound wave is absorbed at the other end of the crystal, resulting in a travelling wave instead of a standing wave. The AOMs are typically operated in the Bragg regime, where most of the power is deflected to the first diffraction order. In this regime, the incident and the refractive angles are identical, this angle is called Bragg's angle. Bragg's angle θ_B is given by Bragg's law

$$\sin\theta_B = \frac{\lambda}{2n\lambda_s}, \tag{3.2}$$

where λ_s is the wavelength of the sound wave, while n is the refractive index of the crystal without modulation. The first order diffraction also experiences a frequency shift equal to the frequency of the sound wave. The frequency and power of the diffracted beam can be controlled by the frequency and power of the RF signal.

3.1.5 Light sources on object plane

To implement our technique in one dimension, a point-like light source is not required. We use a diaphragm with four pair of slits separated by d = 0.25, 0.5, 0.75 and 1 mm (3B Scientific U14101) as the light sources. The width of each slit is 150 μm. The slits are placed such that the long edge is orthogonal to the displacement. The signal beam is modulated by an AMO operating at 40 MHz. The modulated beam is collimated to about 5 mm diameter before being sent to the diaphragm, so that the power distribution is relatively uniform for all the positions of the slits and the little variance of the optical power does not effect the overall results. To generate spatially incoherent light, we place a paper card right in front of the slits. During the acquisition time, the paper card is moved in the transverse plane by a motorized translation stage to average over the incoherent light statistics. The optical power transmitted through each pair of slits is ~ 200 μW for coherent case, and ~ 10 μW for incoherent case.

3.1.6 Generation of incoherent light

To generate incoherent light from the laser beam, we introduce random spatial phase distribution by transmitting the laser beam through a thick paper card. Different points of the card introduce random optical phases to the beam depending on the structure of the card, therefore the spatial field is highly uncorrelated. This transmitted beam shows an static speckle pattern. To average all the speckle patterns, we move the card in the transverse plane by attaching it to a translation stage with two pieces of metal sticks. The translation stage is attached to a stepper motor, whose motion speed and travel distance are programmed by a microcontroller (Arduino Uno). An example code and tutorial can be found on the Sparkfun website[27]. The microcontroller sends the control sequences to a stepper motor driver (Sparkfun ROB-12779), which converts the control sequences to a readable form by the stepper motor. The translation stage moves back and forth by a few millimetres in each motion circle. If the motor moves too fast, it may skip a few steps in each motion circle, resulting the translation stage to slide to one direction. Manual adjustments are required when the accumulated slide distance is comparable to the maximum travel distance of the translation stage.

3.1.7 Mode matching

Mode matching between LO and signal beam is crucial for optical heterodyne detection. To achieve best mode matching, we adjust the signal beam profile by two separate optical telescopes to match the beam size and divergence of LO. In this stage, we prepare LO in TEM_{00} and use a coherent signal beam. Once we obtain maximum interference visibility between LO and signal, we adjust the temperature of the monolithic cavity and switch LO to TEM_{01}. By slightly adjusting the direction of LO and minimizing the interference visibility, we achieve optimal mode matching between signal and LO in TEM_{01}.

3.1.8 Optical path design

The modulated signal beam transmits through the slits. The diffracted light propagates in free space for about $L = 84$ cm and passes through an iris before the objective lens. The measurement error of L is on the scale of millimetres, which is negligible considering that L is almost a metre and is the denominator when calculating the numerical aperture. This distance is sufficient for far-field approximation, since $L \gg W^2/\lambda = 2.88$cm, where $W = 0.15$ mm is the width of each slit. We use the iris to adjust the numerical aperture of the imaging system. Due to the macroscopic separation of the slits, we minimize the numerical aperture to demonstrate that our technique can work below Rayleigh limit. The iris size is measured under an optical microscope with a vernier scaler and the diameter is measured to be 0.8 ± 0.1 mm, which corresponds to a numerical aperture of 0.48×10^{-3} and a Rayleigh distance of 0.99 mm. This is a relatively rough estimation, we subsequently use the experimental data to estimate the iris size with higher precision. The measurement error associated with the diameter of the iris is less than 10% with this rough estimation, and does not harm the result that we can achieve super-resolution well-below the Rayleigh limit. The light transmitted through the objective lens is then mode matched with the LO and subjected to heterodyne detection.

3.1.9 Detection

We use a commercial balanced detector (Thorlabs PDB150A-SP) for heterodyne detection. The bandwidth is set to 50 MHz with a corresponding gain of 10^4 A/W, enabling it to operate at low optical power. To average the heterodyne detector output, which is at 40 MHz, over the acquisition time, we acquire output power of the detector on a spectrum analyser set to zero span at 40 MHz with a resolution bandwidth of 1 kHz and a video bandwidth of 100 Hz. The sweep time is set to be 50 ms for coherent light and 500 ms for incoherent light. One hundred traces on the spectrum analyser are averaged for each measurement.

3.2 Measurement procedure

We first measure the position of a single slit in both coherent and incoherent cases. We cover all but one slit with thick black cards, so that the light can only transmit through one slit. We place the slit on a translation stage with precision of 10 μm and record output power from heterodyne detector at each position for a $\sim$5 mm travel distance.

For the coherent case, we measure the signal power at each position only once except for a small region around $x = 0$. This is because the signal in coherent case shows little fluctuation. We measure the signal ten times at each position around the centre to estimate the stochastic experimental error. This is used to calculate Fisher information for small displacement.

For incoherent light, the signal light exhibits a time dependent speckle pattern, as the paper card moves in front of the slits. We observe large fluctuations on the signal due to the change of the speckle pattern. The fluctuations are reduced by averaging the detector output over time. We take three measurements at each position to estimate the stochastic experimental error.

At last, we measure the separation distance between two slits with incoherent light. Each pair of slits is centered at $x = 0$. The output signal is averaged to reduce fluctuations associated with incoherent light and twelve measurements are made for each pair of slits to estimate experimental error. To compare our result with direct imaging, we use a CCD camera to take the images of each pair of slits with the same objective lens and iris size.

Chapter 4

Results and discussion

We see an excellent agreement between the experimental results and our theoretical prediction. With heterodyne detection in TEM_{01}, we can measure the single slit position within 0.0015 and 0.012 of Rayleigh limit in coherent and incoherent cases, respectively. We can determine the separation of two incoherent light sources located within 0.019 of Rayleigh limit.

4.1 Single slit position measurement

Our technique is sensitive to single slit position measurement.

4.1.1 Coherent case

The result for single slit position measurement with coherent light is shown is Figure 4.1. The detector output is converted to electronic power. The dots are the experimental data while the solid line shows the fitting to the experimental data. The inset shows the detector output around $x = 0$, roughly corresponding to the red circle in the main plot. The error bars show the standard deviations of experimental data at each position. We fit the experimental data to our theoretical predictions by varying both vertical scale and iris size, taking into account of the finite width of the slit. Here we measure the iris size by fitting the heterodyne signal to the theoretical prediction. The fitting results to different data sets show great agreement. The diameter of the iris is calculated to be 0.87 ± 0.01 mm. This value is used for data analysis in the rest of the chapter. This diameter corresponds to a numerical aperture of 0.52×10^{-3} and a Rayleigh distance of 0.912 mm.

To estimate the performance of our technique, we analyse the stochastic error around $x = 0$. Two different types of experimental imperfections contribute to this error. First, mode matching between LO and signal is imperfect, which is affected by air movements and vibrations of optics.

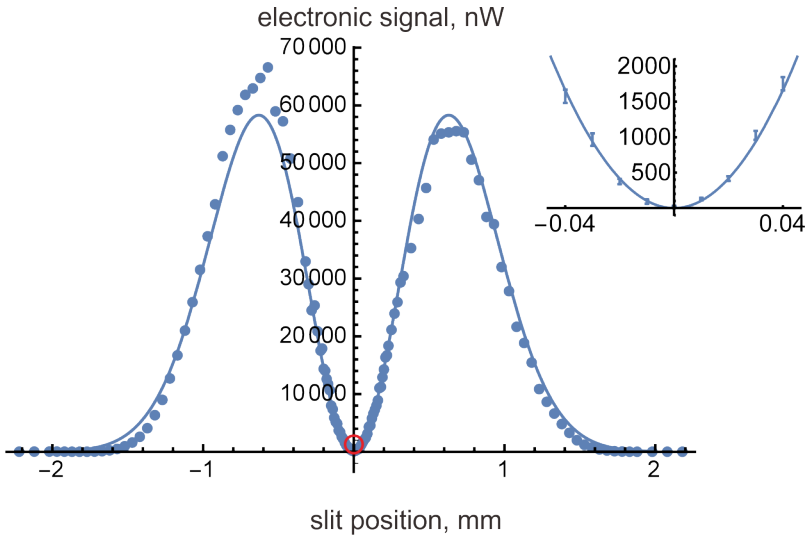

Figure 4.1: Single slit position measurement in coherent case.

This results in a constant fluctuation of detector output at each position of the slit. Second, the power of LO fluctuates due to the instability of the PDH lock. Because the heterodyne signal is proportional to the product of signal and LO amplitudes, the fluctuations of LO power are mapped directly to the fluctuations of detector output, proportional to the signal power. Considering these two types of effects, which can be treated independently from each other, we model the error of our experiment by

$$\sigma_\varepsilon^2 = c^2 + (gP)^2, \tag{4.1}$$

where c is the error due to imperfect mode matching and gP is due to the fluctuations of the power of LO with a fitting parameter g.

We use the above model and fitting parameters to calculate Fisher information and the corresponding Cramér-Rao bound of our measurements. To this end, we suppose the position of the slit is unknown, and we estimate it by the heterodyne signal. According to central limit theorem[28], we suppose the heterodyne signal obeys Gaussian distribution with an unknown parameter x_p

$$f(P,x_p) = \frac{1}{\sqrt{2\pi}\sigma_\varepsilon} e^{-[P-P(x_p)]^2/2\sigma_\varepsilon^2}. \tag{4.2}$$

The Fisher information is

$$I(x_p) = \int_{-\infty}^{+\infty} \left[\frac{\partial f(P,x_p)}{\partial x_p}\right]^2 \Big/ f(P,x_p)\, dP. \tag{4.3}$$

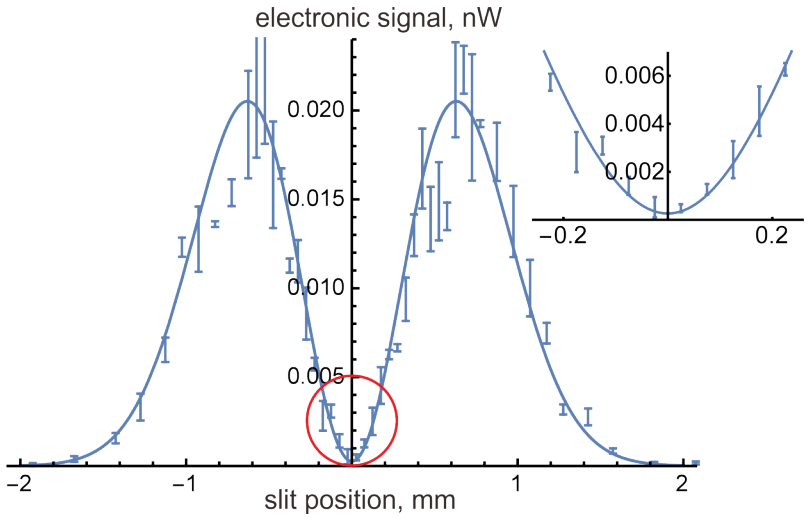

Figure 4.2: Single slit position measurement in incoherent case. Solid line: fitting of the experimental data.

In the neighbourhood of $x_p = 0$, the output power $P(x_p)$ is a quadratic function of x_p, $P(x_p) = ax_p^2$, with a variance according to equation 4.1. With the constants a, c and g acquired from experimental data, we find the Fisher information in the limit of $g \ll 1$

$$I(x_p) = \frac{4a^2x_p^2}{a^2g^2x_p^4 + c^2}. \tag{4.4}$$

Next, we calculate the slit position where the Fisher information reaches its maximum, by taking the derivative of $I(x_p)$ with respect to x_p. We find $I_{max} = 2a/gc$ at $x_p = \sqrt{c/ag}$. For the coherent position measurement data, Fisher information reaches maximum at $x_p = 0.012$ mm. From the corresponding Cramér-Rao bound, we find the uncertainty of the measurement to be $\delta x_p = \sqrt{Var(x_p)} \geq \frac{1}{\sqrt{I(x_p)}} = 1.4\mu m$. This means the best precison we can get is 0.0015 of Rayleigh limit.

4.1.2 Incoherent case

The result for single slit position measurement with incoherent light is shown is Figure 4.2. The inset also shows the detector output around $x = 0$, roughly corresponding to the red circle in the main plot. The error bars show the standard deviation of the experimental data and the solid line is the fitting to the data by varying the signal power and iris size. We see a nice agreement between

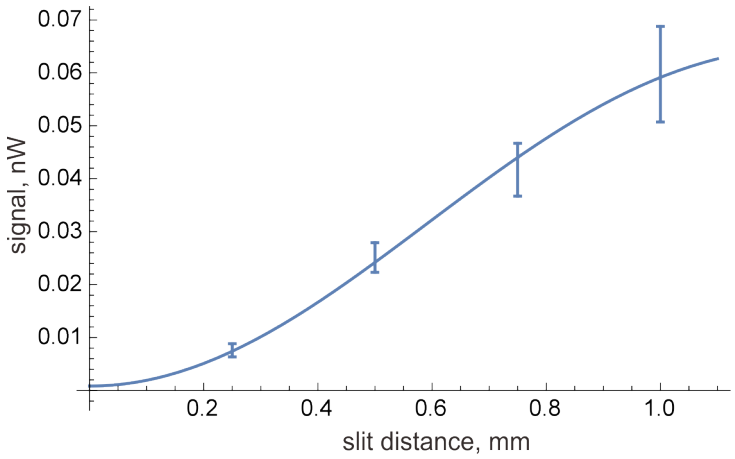

Figure 4.3: Double slit separation measurement with incoherent light.

theoretical prediction and experimental data.

When taking the data, we observe that without averaging, the fluctuations of the heterodyne signal are comparable to the signal itself. For the averaged data, this effect is significantly reduced, but it still dominates the error at high signal power. The error bars in the plot show the standard deviation of heterodyne signal at each position. The standard deviation is significantly larger than that in the coherent case, as we expected. In the vicinity of $x_p = 0$, the error model in equation 4.1 is still valid, while the parameters should be adjusted accordingly.

We calculate Fisher information and Cramér-Rao bound in the same way as for the coherent case. Fisher information reaches its maximum at x_p = 0.14 mm, corresponding to δx_p = 11 μm. This result shows that we can locate the slit with a precision of 0.012 of Rayleigh limit.

4.2 Separation of two slits

At last, we measure the distance between two slits separated below Rayleigh limit. The results are shown in Figure 4.3. The output power is measured when the centres of each pair of slits are at position $x_p = 0$. The error bars show the standard deviation of twelve measurements. The experimental error increases with detector output power, as we expected. For incoherent light, the heterodyne signal follows similar patterns for both single-slit and double-slit measurements.

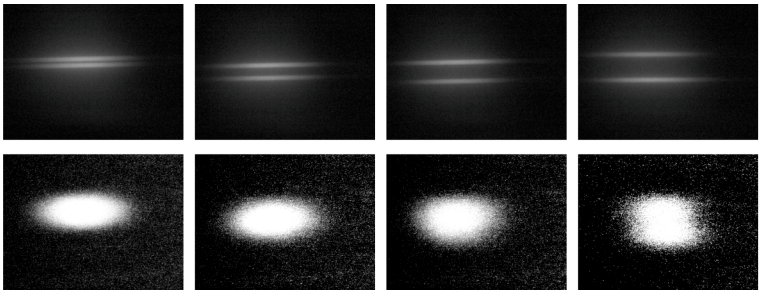

Figure 4.4: Direct imaging result on a CCD camera

Therefore, we can calculate the Fisher information in the similar way using the error model in equation 4.1. The Fisher information reaches maximum at $d = 0.18$ mm, corresponding to a Cramŕ-Rao bound of $\delta d = 17$ μm. Our technique has a precision up to 0.019 of Rayleigh limit.

To show the advantage of our technique, we compare our results with direct imaging. We take images of each pair of slits with the same optical imaging system on a CCD camera. The images are shown in Figure 4.4. The distances between the slits are $d = 0.25$, 0.50, 0.75, 1.00 mm, from left to right. The top row shows the images without iris. The diameter of the objective lens is 25.4 mm, corresponding to a numerical aperture of 1.51×10^{-2} and a Rayleigh limit of 31.5 μm. The four pairs of slits are clearly resolved. However, when the iris is inserted in front of objective lens, the numerical aperture reduces by more than 30 times. The pairs of slits are not resolved for $d < 1$ mm, as is shown in the bottom row.

4.3 Discussion

We have shown in section 4.1 that the Fisher information in our experiment decreases to zero as d goes to zero. We can improve the measurement precision by reducing fluctuations of mode matching with more stable optics. We can also use spatial light modulators to prepare the LO in the desired mode to increase the stability of LO power. However, the fundamental limit to the precision of our technique is the shot noise, which comes from the quantum feature of light. This can be suppressed by using squeezed light. The photon counting method gives the photon statistics. In practice, detector dark counts will affect the photon statistics, therefore reducing the precision

of measurements.

After finishing our experiments, we found a similar implementation for displacement measurement of coherent beam by Hsu *et al.*[29]. Hsu *et al.* proposed to use homodyne detection with a LO in TEM_{01} to measure small displacement of a coherent beam in TEM_{00}, which is very similar to our technique to measure single slit position with coherent light. They analysed such measurement theoretically and found that in the limit of small displacement, it could reach the quantum limit.

A Gaussian beam in TEM_{00} displaced by distance d has amplitude profile

$$u_0(x-d) = \left(\frac{2}{\pi w_0^2}\right)^{1/4} e^{-\left(\frac{x-d}{w_0}\right)^2}, \tag{4.5}$$

where w_0 is the beam waist. The photon position distribution is therefore

$$P(x) = \left(\frac{2}{\pi w_0^2}\right)^{1/2} e^{-2\left(\frac{x-d}{w_0}\right)^2}. \tag{4.6}$$

The quantum optimal measurement of displacement of a coherent TEM_{00} beam can be achieved by calculating the mean position of the detected photons. The sensitivity of such measurement can be defined as the derivative of the mean position with respect to the displacement divided by the standard deviation. In this case, the quantum limit of the sensitivity is

$$S_{QL} = \frac{1}{\Delta d_{QL}} = \frac{2\sqrt{N}}{w_0}, \tag{4.7}$$

where N is the number of detected photons. For balanced homodyne detection with a LO in TEM_{01}, Hsu *et al.* found the output of the homodyne detector, which is the difference of the photocurrent of the two photodiodes, is

$$\hat{n}_- = \sqrt{N_{LO}}\left(\frac{2\sqrt{N}}{w_0}d + \delta\hat{X}\right), \tag{4.8}$$

where $\delta\hat{X} = \delta a + \delta a^\dagger$ is the amplitude quadrature noise operator of the TEM_{01} component of the signal beam and N_{LO} is the photon number of the LO. For coherent state, when $d \ll w_0$, the sensitivity of homodyne detection is[29]

$$S_{HD} = \frac{2\sqrt{N}}{w_0}, \tag{4.9}$$

which is the same as the quantum limit. Therefore homodyne detection with a LO in TEM_{01} is a quantum optimal measurement for displacement of a coherent beam. Hsu *et al.* also argued by introducing squeezing to the signal beam, one can reach sensitivity higher than this quantum limit. However, Hsu *et al.* did not realise their setup in experiments and focused only on coherent light. Our experiments prove the validity of their proposal and extend the scope to super-resolution with incoherent light.

We can also interpret such analysis in terms of Fisher information. For a small displacement, the Gaussian mode can be approximated as follows

$$\begin{aligned} u_0(x-d) &= u_0(x) - d \cdot u_0'(x) \\ &= u_0(x) + \frac{d}{w_0} u_1(x). \end{aligned} \tag{4.10}$$

where $u_0'(x)$ is the derivative of $u_0(x)$ and $u_1(x)$ is the profile of TEM_{01}. With a small displacement, TEM_{01} is illuminated with an amplitude that is d/w_0 of the amplitude of TEM_{00}. If we assume the TEM_{00} beam to be in coherent state $|\alpha\rangle$, the state of TEM_{01} is therefore $|\frac{d}{w_0}\alpha\rangle$. Performing homodyne detection with a LO in TEM_{01}, we can measure the quadrature distribution of $|\frac{d}{w_0}\alpha\rangle$. Without loss of generality, we can assume α to be real, the probability distribution of quadrature x is

$$P(x,d) = \left| \left\langle x \middle| \frac{d}{w_0}\alpha \right\rangle \right|^2 = \frac{1}{\sqrt{\pi}} e^{-\left(x - \frac{d}{w_0}\sqrt{2}\alpha\right)^2}. \tag{4.11}$$

The Fisher information to estimate d is

$$\begin{aligned} I_\alpha(d) &= E\left[\left(\frac{\partial}{\partial d} \log P(x,d) \right)^2 \right] \\ &= -E\left[\left(\frac{\partial^2}{\partial d^2} \log P(x,d) \right) \right] \\ &= -E\left[-4\frac{\alpha^2}{w_0^2} \right] \\ &= 4\frac{\alpha^2}{w_0^2} \end{aligned} \tag{4.12}$$

For coherent state $\alpha = \sqrt{N}$ where N is expectation of photon number. Noticing that $w_0 = 2\sigma$, we

can rewrite the Fisher information as

$$I_\alpha(d) = \frac{N}{\sigma^2} = S_{QL}^2. \tag{4.13}$$

The single photon Fisher information is

$$I(d) = \frac{1}{\sigma^2}. \tag{4.14}$$

This is the same as quantum Fisher information in equation 2.35, which gives the shot noise limit of displacement measurement. From this result, we can conclude that our single slit position measurement with coherent light is quantum optimal for small displacement, when no experimental error is presented.

To measure the displacement of a single beam, one can also measure the mean position of all the photons in this beam. This is the same technique as direct imaging. If the position of each photon can be measured with arbitrary precision, the Fisher information can be calculated using equation 2.29. In this case, $\Lambda(x)$ is given by

$$\Lambda(x) = |\psi(x-d)|^2, \tag{4.15}$$

where $\psi(x)$ is given by equation 2.32. The single photon Fisher information to estimate d is

$$I(d) = \frac{1}{\sigma^2}, \tag{4.16}$$

which also equals the quantum limit. But this Fisher information cannot be obtained in experiments due to the finite size of the pixels on the detector. Any displacement smaller than the pixel size cannot be detected, which sets a fundamental limit for the precision of displacement measurement. However, homodyne detection with a LO in TEM_{01} is not restrict by such limit in experiments, and it can reach the quantum limit in practice.

To estimate the centroid and separation of two coherent beams displaced by $\pm d$, the Fisher information depends on the relative phase of the two beams. If the two beams are in phase, the beam profile is

$$u_0(x-d) + u_0(x+d) = u_0(x) - d \cdot u_0'(x) + u_0(x) + d \cdot u_0'(x) = 2u_0(x). \tag{4.17}$$

No information is contained in TEM_{01}. However, if the two beams are out of phase

$$e^{i\pi}u_0(x-d)+u_0(x+d)=-u_0(x)+d\cdot u_0'(x)+u_0(x)+d\cdot u_0'(x)=2\frac{d}{w_0}u_1(x). \tag{4.18}$$

The amplitude is TEM_{01} is doubled and more information can be obtained. Without *a priori* knowledge of the phase, we cannot determine the Fisher information.

For incoherent light, the TEM_{00} beam is described by the intensity profile

$$U_0(x)=u_0(x)^2=\left(\frac{2}{\pi w_0^2}\right)^{1/2}e^{-2\left(\frac{x}{w_0}\right)^2}. \tag{4.19}$$

where d is the displacement of one light source and $w_0=2\sigma$, σ being the width of the point spread function. For two TEM_{00} beams displace by $\pm d$, the intensity profile is give by

$$\begin{aligned}U&=|u_0(x-d)|^2+|u_0(x+d)|^2\\&=[u_0(x)-\frac{d}{w_0}u_1(x)]^2+[u_0(x)+\frac{d}{w_0}u_1(x)]^2\\&=2u_0(x)^2+2\frac{d^2}{w_0^2}u_1(x)^2\\&=2[U_0(x)+\frac{d^2}{w_0^2}U_1(x)].\end{aligned} \tag{4.20}$$

For two incoherent beams, with small displacement $\pm d$, TEM_{01} is illuminated with intensity $\frac{d^2}{w_0^2}$ of the total intensity of the two TEM_{00} beams. We can use homodyne detection with a LO in TEM_{01} to measure TEM_{01} component of the signal beam. Assume the total intensity of two TEM_{00} beams to be I_0, the intensity of TEM_{01} is $I_1=\frac{d^2}{w_0^2}I_0$. If we average the homodyne output, the intensity of TEM_{01} is measured directly. The output signal of the homodyne detector is

$$P=\frac{\theta_2^2}{4w_0^2}I_0, \tag{4.21}$$

where $\theta_2=2d$ is the separation between the two beams. The output signal can be used to estimate θ_2.

Chapter 5

Application to imaging

In our experiment, we performed heterodyne detection with only one Hermite-Gaussian mode TEM_{01}. The result is sufficient to measure the separation distance of two incoherent light sources significantly below Rayleigh limit. By engaging more TEMs, we can further improve the resolution and apply our technique to full imaging.

5.1 Heterodyne detection in higher Hermite-Gaussian modes

In chapter 2, we derived the output current from a heterodyne detector with a LO in TEM_{01}. In this section, we generalise our result to a LO in any Hermite-Gaussian mode for an extended object. A Gaussian transfer function is assumed for the calculations. The heterodyne detector output with a LO in TEM_{0n} for an extended light source is

$$J_{0n} = \int_{-\infty}^{+\infty} E(x)J(x)\,dx, \tag{5.1}$$

where $J(x)$ is the response of heterodyne detector to a point source at x defined by equation 2.52. The field distribution of LO in TEM_{0n} is

$$E_{LO,n}(x) = \frac{H_n(x/\sqrt{2}\sigma)}{(2\pi)^{1/4}\sqrt{2^n n!\sigma}} e^{-x^2/4\sigma^2}, \tag{5.2}$$

where $H_n(\cdot)$ is the Hermite polynomial. Noticing that equation 2.52 is a Weierstrass transform of the Hermite polynomial, we can simplify the expression of $J(x)$ as

$$J_n(x) = \frac{1}{\sqrt{n!}} \left(\frac{x}{2\sigma}\right)^n e^{-x^2/8\sigma^2}. \tag{5.3}$$

We see that, for objects of size $< \sigma$, photocurrent J_{0n} approximates the nth moment of the field in the object plane.

5.2 Hermite-Gaussian Microscopy

We propose a new imaging technique for coherent light in this section. The current $J_{0n}(x)$ is proportional to the component of $E(x)$ in TEM_{0n}. Measurement with LO in all Hermite-Gaussian modes performs a decomposition of $E(x)$ in the Hermite-Gaussian basis. This allows us to reconstruct the full image with a resolution beyond Rayleigh limit. We can write $E(x)$ in the Hermite-Gaussian basis with coefficients β_k as

$$E(x) = \sum_{k=0}^{\infty} \beta_k H_k\left(\frac{x}{2\sigma}\right) e^{-x^2/8\sigma^2}. \tag{5.4}$$

We can calculate coefficients β_k to reconstruct field distribution $E(x)$ as follows. Let us write Hermite polynomial of degree k as

$$H_k(x) = \sum_{n=0}^{k} \alpha_{kn} x^n, \tag{5.5}$$

where α_{kn} are the coefficients of the Hermite polynomial. The coefficients β_k become

$$\begin{aligned}
\beta_k &= \int_{-\infty}^{+\infty} E(x) H_k\left(\frac{x}{2\sigma}\right) e^{-x^2/8\sigma^2}\, dx \\
&= \int_{-\infty}^{+\infty} E(x) \sum_{n=0}^{k} \alpha_{kn} \left(\frac{x}{2\sigma}\right)^n e^{-x^2/8\sigma^2}\, dx \\
&= \sum_{n=0}^{k} \sqrt{n!}\,\alpha_{kn} \int_{-\infty}^{+\infty} E(x) J(x)\, dx \\
&= \sum_{n=0}^{k} \sqrt{n!}\,\alpha_{kn} J_{0n}.
\end{aligned} \tag{5.6}$$

After acquiring J_{0n} in experiments, we can use equation 5.6 to calculate coefficients β_k, and subsequently reconstruct $E(x)$ from equation 5.4. We name such imaging technique Hermite-Gaussian microscopy (HGM). This technique allows us to reconstruct the image with arbitrary resolution when sufficiently many Hermite-Gaussian modes are engaged in experiment. In practice, the first few tens of Hermite-Gaussian modes can be obtained using spatial light modulators (SLMs). We compare HGM with direct imaging in Figure 5.1. The first twenty one Hermite-Gaussian modes are used for HGM in this comparison. Two point light sources are separated by Rayleigh limit,

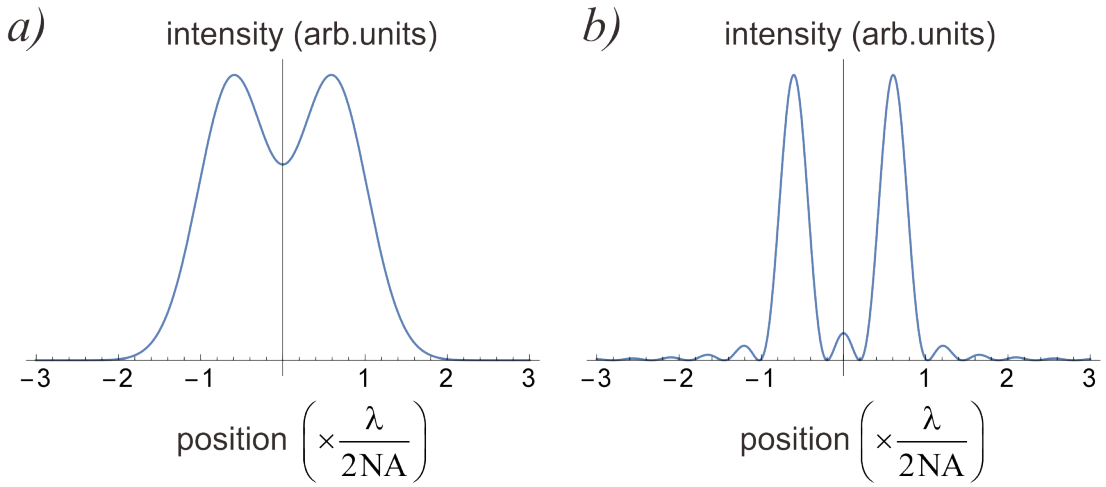

Figure 5.1: Comparison of direct imaging and HGM. a): Direct imaging result. b): HGM result with TEM_{00} to $\mathrm{TEM}_{0,20}$.

and the point spread function is approximated by Gaussian function. We can see a significant improvement on resolution.

When two light sources are separated by Rayleigh limit, the intensity in the image plane at the centre is $\sim 26.3\%$ less than the maximum intensity. Following this feature, we define the resolution of HGM as the distance between two objects when the image intensity in the centre is 75% of the maximum intensity. In Figure 5.2, we plot the resolution as a function of the number of Hermite-Gaussian modes used in HGM. The resolution increases dramatically when we begin to include higher-order Hermite-Gaussian modes. Above a certain threshold, including higher modes ceases to provide much benefit, but brings technical challenges in experiments.

We can easily extend HGM to two dimensions by varying both indices of TEM_{mn}. After measuring the photoncurrent J_{mn}, we can apply the same algorithm to reconstruct field distribution $E(x,y)$.

5.3 Hermite-Gaussian microscopy for incoherent light sources

For more general applications, we can extend HGM to incoherent light. We demonstrate the reconstruction algorithm in one dimension. In this case, since we can only observe the intensity of

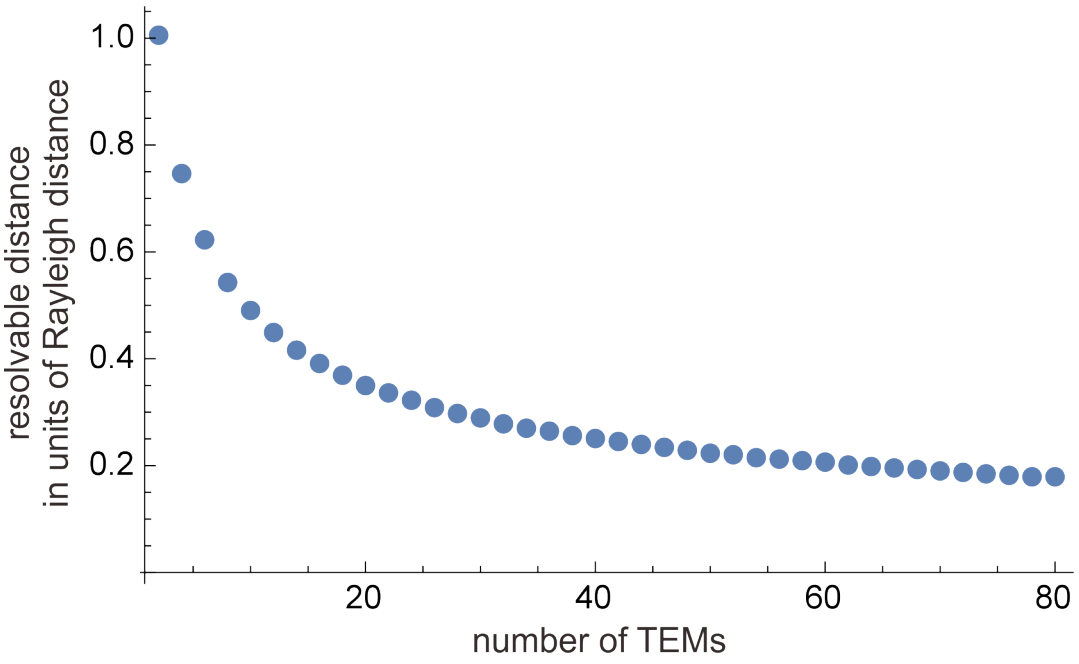

Figure 5.2: Resolution of HGM as a function number of Hermite-Gaussian modes used.

the light field instead of amplitude, the average power of the detector output should be used for image reconstruction. The output power from heterodyne detector is

$$\begin{aligned}\langle P\rangle \propto \langle J_{0n}^2\rangle &= \int_{-\infty}^{+\infty} \langle E(x_1)E(x_2)\rangle\, J(x_1)J(x_2)dx_1dx_2 \\ &= \int_{-\infty}^{+\infty} I(x)J^2(x)dx \\ &= \int_{-\infty}^{+\infty} I(x)\frac{1}{n!}\left(\frac{x}{2\sigma}\right)^{2n} e^{-x^2/4\sigma^2}\,dx.\end{aligned} \tag{5.7}$$

We obtain only even moments of the field distribution, which means we can obtain only the even coefficients of the decomposition of $I(x)$ in the Hermite-Gaussian basis. In this case, a "ghost" image $I(-x)$ is added to the original image, and we recover $\frac{1}{2}[I(x)+I(-x)]$. For two-dimensional microscopy, three ghost images, $I(x,-y), I(-x,y), I(-x,-y)$, are added to the original image $I(x,y)$. We can resolve the original image by avoiding the overlap between the original and ghost images. In practice, we can place the object in a single quadrant of the $x-y$ plane, whose origin and axes are defined by the Hermite-Gaussian modes.

5.4 Comparison of HGM and optical state tomography

We can compare HGM with optical state tomography (OST)[30]. In quantum optics, the optical field is described by a harmonic oscillator, which can be decomposed in Fock basis. The wave-function of the n-photon Fock state in position basis is also given by Hermite-Gaussian polynomial of degree n

$$\psi_n(x) = \frac{1}{\pi^{1/4}\sqrt{2^n n!}} H_n(x) e^{-x^2/2}. \tag{5.8}$$

In OST via balanced homodyne detection, the density matrix of the optical state is usually reconstructed in the Fock basis. In the inverse linear transformation reconstruction method, the pattern functions in Fock basis are calculated. The elements of the density matrix can be calculated through the pattern functions[22] and the quadrature distributions, which are obtain from the homodyne output current. We can reconstruct the optical state to the desired precision by truncating the Fock basis to the corresponding photon number. In HGM, the Fock basis is replace by Hermite-Gaussian modes, which have the same mathematical expression. The reconstruction method is in analogy to OST.

Chapter 6

Conclusion and outlook

6.1 Summary

Microscopes are of great importance for biology and astronomy research. Since the invention of microscopes in the 16th century, scientists have put numerous efforts to increasing the resolution of microscopes. In late 19th century, Ernst Abbe and Lord Rayleigh discovered the resolution limit of an imaging system due to diffraction of light. This fundamental restriction has been an unbreakable rule for microscope design for more than a century. Microscopy resolution is improved mainly by using shorter wavelength such as in scanning electron microscopy, or larger numerical aperture by oil immersion of objective lens. Successful attempts to achieve sub-Rayleigh resolution have emerged in the last few decades. Those techniques circumvent Rayleigh criterion by nonlinear optics, near-field optics or photo-switchable fluorephores. All these new techniques contributed significantly to biology research. However, a new technique with linear optics in far-field remains an important problem.

By interpreting the far-field image with quantum optics, Tsang *et al.* show that there is no resolution limit in a quantum optimal measurement of the image in far-field, rendering Rayleigh criterion irrelevant to separation estimation of incohrent light sources. Tsang *et al.* subsequently proposed a quantum optimal measurement by counting photon numbers in each Hermite-Gaussian mode. With this method, one can approach quantum Cramér-Rao bound asymptotically. The experimental setup for this measurement is sophisticated and difficult to implement in experiments.

Inspired by the proposal by Tsang *et al.*, we propose an alternative way to measure optical field in each Hermite-Gaussian mode via optical heterodyne detection. Taking advantage of the fact that heterodyne detection is only sensitive to the local oscillator mode, we can separate the components of the optical field in the Hermite-Gaussian basis. This technique is implemented with

TEM_{01}. We first meausre the position of a single slit with coherent and incoherent light, respectively. The precision is within 0.0015 and 0.012 of Rayleigh limit. Subsequently, we apply our technique to measure the distance between two incoherent light sources within 0.019 of Rayleigh limit. Our technique can be implemented with a relatively simple setup and low cost, which is a great advantage over the existing super-resolution techniques.

After demonstration of plausibility of our technique with TEM_{01}, we theoretically analyse the technique with higher Hermite-Gaussian modes. The result shows that we can acquire full image of an object emitting coherent and incoherent light below Rayleigh limit. This method is reminiscent to optical state tomography with decomposition in Fock basis.

6.2 Outlook

We demonstrate our method with macroscopic objects and a low numerical aperture of $\sim 10^{-3}$. In the future, we plan to implement our technique with microscopic objects with a dimension of ~ 100 nm and a numerical aperture of ~ 1. This numerical aperture is typical in the state-of-the art microscopes. A resolution on nanometer scales can be expected.

We will include more Hermite-Gaussian modes in our measurements. The LO is currently prepared in TEM_{01} by a monolithic cavity. The transmission through the cavity decreases significantly with the order of TEMs, limiting the Hermite-Gaussian modes attainable with our setup. On the contrary, SLMs do not suffer from such problems. Two SLMs can be used to prepare the LO in the desired TEM, with one modulating the spatial distribution, the other modulating the phase of the optical field. We will reconstruct full image of an object by engaging higher orders of TEMs. Due to the similarity of HGM with OST, successful results can be expected.

6.3 New progress in this field

After Tsang *et al.* proposed SPADE, they found another measurement method, named super localization by image inversion interferometry (SLIVER), to achieve sub-Rayleigh resolution[31].

The imaged is sent through an inversion interferometer, so that the inverted image is overlapped with the original image. Therefore the field distribution of the original image $E(x)$ is separated into symmetric component $E_s(x)$ and antisymmetric component $E_a(x)$. Two photodetectors collect spatially-unresolved photons in the symmetric and antisymmetric components. The photocurrent detected in M detection windows are processed to get the estimate of the separation distance. Since one can obtain both amplitude and phase information of the image, Fisher information remains constant regardless of the separation distance. This proposal, together with the original SPADE proposal, has sparked various implementations of super-resolution. SLIVER has been implemented recently by Zhang et al.[32] and inspired the work by Tham *et al.*[33]. Paur *et al.*[34] realised an implementation inspired by SPADE. We expect more progress in this field.

Appendix A

Quantum description of weak thermal sources

We describe the light in the image plane with quantum optics by assuming quasi-monochromatic paraxial light with one polarization. We denote the multimode complex amplitude as a column vector $\alpha = (\alpha_1, \alpha_2, ..., \alpha_J)^T$ and $\alpha^\dagger = (\alpha_1^*, \alpha_2^*, ..., \alpha_J^*)$ as the conjugate transpose of α, where α_j is the complex amplitude of the jth mode. $|\alpha\rangle = |\alpha_1\rangle |\alpha_2\rangle ... |\alpha_J\rangle$ is the multimode coherent state with complex amplitude α. According to Sudarshan-Glauber representation[18], any multimode optical state with density matrix ρ can be expressed in terms of P representation[19],

$$\rho = \int P(\alpha) |\alpha\rangle \langle\alpha| d^2\alpha, \tag{A.1}$$

where $d^2\alpha = \prod_{j=1}^{n} d\,\mathrm{Re}(\alpha_j) d\,\mathrm{Im}(\alpha_j)$.

The P representation of thermal light is given by a multivariate Gaussian distribution with complex variate α of zero mean[19]

$$P(\alpha) = \frac{1}{det(\pi\Gamma)} e^{-\alpha^\dagger \Gamma^{-1} \alpha}, \tag{A.2}$$

where $\Gamma = E[\alpha\alpha^\dagger]$ is covariance matrix of α with phase space distribution $P(\alpha)$, which can be interpreted as the correlation function in quantum optics. $E[\cdot]$ is defined by

$$E[f(\alpha)] = \int P(\alpha) f(\alpha) d^2\alpha, \tag{A.3}$$

which is the expectation value of an arbitrary function $f(\alpha)$ with phase space distribution $P(\alpha)$. Because the complex amplitudes α_j of different modes are not statistically independent in general for thermal light[19], Γ is not necessarily diagonal.

We can calculate the matrix element of ρ in multimode Fock basis $|n\rangle = |n_1\rangle |n_2\rangle ... |n_J\rangle$, where

$n = \sum_j n_j$, as follows.

$$\begin{aligned}\langle m_1, m_2, ...m_J| \rho |n_1, n_2, ..., n_J\rangle &= \int P(\alpha) \langle m_1, m_2, ...m_J|\alpha_1, \alpha_2, ..., \alpha_J\rangle \langle \alpha_1, \alpha_2, ..., \alpha_J|n_1, n_2, ..., n_J\rangle d^2\alpha \\ &= \int P(\alpha) e^{-|\alpha|^2} \prod_j \frac{\alpha_j^{m_j} (\alpha_j^*)^{n_j}}{\sqrt{m_j! n_j!}} d^2\alpha \\ &= \frac{e^{-|\alpha|^2}}{\sqrt{m_1! m_2! ... m_J! n_1! n_2! ... n_J!}} E[\prod_j \alpha_j^{m_j} (\alpha_j^*)^{n_j}]\end{aligned} \tag{A.4}$$

According to Gaussian moment theorem for complex variates[19], if $\sum_j m_j \neq \sum_j n_j$,

$$E[\prod_j \alpha_j^{m_j} (\alpha_j^*)^{n_j}] = 0. \tag{A.5}$$

Therefore $\langle m| \rho |n\rangle = 0$, if $m \neq n$. The density matrix of thermal state can be written as an incoherent mixture of n-photon Fock state[15]

$$\rho = \sum_{n=0}^{\infty} \pi_n \rho_n, \tag{A.6}$$

where ρ_n is the multimode n-photon Fock state, while π_n is the corresponding probability. Within the short coherence time of thermal state, we assume the average photon number ε at image plane is much smaller than one

$$\varepsilon = \sum_j \mathrm{Tr}\, \rho a_j^\dagger a_j = \sum_j E[|\alpha_j|^2] = E[\sum_j |\alpha_j|^2] = E[|\alpha|^2] \ll 1, \tag{A.7}$$

where a_j and $a_j^\dagger$ are annihilation and creation operators of jth mode. Under this assumption, we calculate the probability of detecting n photons in the image plane within the coherence time. The probability of detecting n photons is given by [19]

$$\pi_n = \mathrm{Tr}(\rho |n\rangle \langle n|) = E\left[\prod_j \frac{|\alpha_j|^{2n_j} e^{-|\alpha_j|^2}}{n_j!}\right], \tag{A.8}$$

Therefore, the probability of detecting zero photon is

$$\pi_0 = E[\prod_j e^{-|\alpha_j|^2}] = E[e^{-\Sigma_j |\alpha_j|^2}] = E[e^{|\alpha|^2}] = 1 - \varepsilon + O(\varepsilon^2). \tag{A.9}$$

The probability of detecting one photon in jth mode is

$$\pi_1^{(j)} = E[|\alpha_j|^2 e^{-|\alpha_j|^2} \prod_{i\neq j} e^{-|\alpha_i|^2}] = E[|\alpha_j|^2 \prod_i e^{-|\alpha_i|^2}] = E[|\alpha_j|^2 e^{-\Sigma_i |\alpha_i|^2}] = E[|\alpha_j|^2 e^{-|\alpha|^2}]. \quad \text{(A.10)}$$

The probability of detecting one photon mulitmode state is

$$\pi_1 = \sum_j \pi_1^{(j)} = \sum_j E[|\alpha_j|^2 e^{-|\alpha|^2}] = E[\sum_j |\alpha_j|^2 e^{-|\alpha|^2}] = E[e^{-|\alpha|^2}|\alpha|^2] = \varepsilon + O(\varepsilon^2). \quad \text{(A.11)}$$

The probability of detecting more than one photon is

$$\sum_{n=2}^{\infty} \pi_n = 1 - \pi_0 - \pi_1 = O(\varepsilon^2), \quad \text{(A.12)}$$

and we can rewrite the density matrix to the leading order of ε,

$$\rho = (1-\varepsilon)\rho_0 + \varepsilon\rho_1. \quad \text{(A.13)}$$

Define $|1_j\rangle = a_j^\dagger |vac\rangle$ as the single photon Fock state in the jth mode, where $|vac\rangle$ is the vacuum state. We can write ρ_1 in terms of $\{|1_j\rangle\}$

$$\begin{aligned}
\langle 1_i|\rho|1_j\rangle &= \langle vac|a_i \rho a_j^\dagger |vac\rangle \\
&= \langle vac|a_i (\int P(\alpha)|\alpha\rangle\langle\alpha| d^2\alpha) a_j^\dagger |vac\rangle \\
&= \int P(\alpha)\langle vac|a_i|\alpha\rangle\langle\alpha|a_j^\dagger|vac\rangle d^2\alpha \\
&= \int P(\alpha)\langle vac|\alpha_i|\alpha\rangle\langle\alpha|\alpha_j^*|vac\rangle d^2\alpha \\
&= \int P(\alpha)\alpha_i\alpha_j^* |\langle\alpha|vac\rangle|^2 d^2\alpha \\
&= \int P(\alpha)\alpha_i\alpha_j^* e^{-|\alpha|^2} d^2\alpha \\
&= E[\alpha_i\alpha_j^* e^{-\alpha^\dagger\alpha}] \\
&= \Gamma_{ij} + O(\varepsilon^2),
\end{aligned} \quad \text{(A.14)}$$

where Γ_{ij} is the matrix element of Γ. From equation A.13 and A.14, we have

$$\langle 1_i|\rho|1_j\rangle = \langle 1_i|[(1-\varepsilon)\rho_0 + \varepsilon\rho_1]|1_j\rangle = \varepsilon\langle 1_i|\rho_1|1_j\rangle, \quad \text{(A.15)}$$

$$\langle 1_i|\rho_1|1_j\rangle = \frac{1}{\varepsilon}[\Gamma_{ij} + O(\varepsilon^2)]. \quad \text{(A.16)}$$

We approximate ρ_1 to the first order of ε, and obtain

$$\rho_1 = \frac{1}{\varepsilon}\sum_{i,j}\Gamma_{i,j}\left|1_i\right\rangle\left\langle 1_j\right|. \tag{A.17}$$

It is easier to calculate Γ using the relation between the correlation function in the image plane and object plane. Let us write the complex amplitude in the object plane as column vector $\alpha^{(O)} = (\alpha_1^{(O)}, \alpha_2^{(O)}, ..., \alpha_K^{(O)})^T$. The modes in the object plane and image plane are not necessarily the same, so J and K can be different. For a linear optical system, the complex amplitudes in the image plane and the object plane is related by a unitary transform

$$\alpha = S\alpha^{(O)}, \tag{A.18}$$

where S is a unitary $J \times K$ matrix, called the field scattering matrix or S-matrix. The correlation function in the image plane and the object plane is related by the S-matrix as follows[19]

$$\Gamma = S\Gamma^{(O)}S^{\dagger}, \tag{A.19}$$

where $\Gamma^{(O)}$ is correlation function on object plane. For two point emitters at positions $u = u_1$ and $u = u_2$, the matrix element of the spatial correlation function in the object plane is

$$\Gamma_{ij}^{(O)}(u,v) = \varepsilon_0\delta_{uv}(\delta_{uu_1} + \delta_{uu_2}), \tag{A.20}$$

where ε_0 is the average photon number of each light source. Here we assume equal brightness of two emitters, and this assumption is used for the rest of the chapter. For point emitters at different positions in the object plane, the S-matrix can be written as a function of position x as $S = S(x)$. According to equation A.19, noticing that S is a unitary matrix, we find the correlation function in the image plane to be

$$\Gamma_{ij} = \varepsilon_0[S_i(x_1)S_j^*(x_1) + S_i(x_2)S_j^*(x_2)], \tag{A.21}$$

where $S_i(x_q) = \sum_k S_{ik}(x_q)$ is the sum of ith row of $S(x_q)$ and $S_j^*(x_q)$ is the complex conjugate of $S_j(x_q)$.

We can define the quantum efficiency of the optical system as

$$\eta = \sum_i |S_i(x_q)|^2. \tag{A.22}$$

Therefore, the photon number on the image plane is $\varepsilon = 2\varepsilon_0\eta$. The multimode single photon state in the image plane can be written as

$$|\psi_q\rangle = \sum_i \psi_{i,x_q} |1_i\rangle, \tag{A.23}$$

where

$$\psi_{i,u_q} = \frac{S_i(x_q)}{\sqrt{\eta}} \tag{A.24}$$

is the wavefunction of the single photon state in the ith mode from emitter u_q. Replacing Γ_{ij} in equation A.17 with equation A.21 and using equation A.23, we can write ρ_1 as follows

$$\begin{aligned}
\rho_1 &= \frac{\varepsilon_0\eta}{\varepsilon} \sum_{i,j} (\psi_{i,x_1}\psi^*_{j,x_1} + \psi_{i,x_2}\psi^*_{j,x_2}) |1_i\rangle \langle 1_j| \\
&= \frac{1}{2} \sum_{i,j} \psi_{i,x_1} |1_i\rangle \langle 1_j| \psi^*_{j,x_1} + \sum_{i,j} \psi_{i,x_2} |1_i\rangle \langle 1_j| \psi^*_{j,x_2} \\
&= \frac{1}{2}(|\psi_1\rangle \langle \psi_1| + |\psi_2\rangle \langle \psi_2|).
\end{aligned} \tag{A.25}$$

Bibliography

[1] E. Abbe, Beiträge zur Theorie des Mikroskops und der mikroskopischen Wahrnehmung, Archiv für Mikroskopische Anatomie, **9** (1): 413468, 1873.

[2] Lord Rayleigh, Investigations in optics, with special reference to the spectroscope, Philosophical Magazine **8**(49): 261-274, 1897.

[3] W. Denk, J. H. Strickler, W. W. Webb, Two-photon laser scanning fluorescence microscopy, Science **248**(4951): 73-76, 1990.

[4] S. W. Hell and J. Wichmann, Breaking the diffraction resolution limit by stimulated emission: stimulated-emission-depletion fluorescence microscopy, Optics Letters, **19**(11): 780-782, 1994.

[5] D. W. Phol, W. Denk and M. Lanz, Optical stethoscopy: Image recording with resolution $\lambda/20$, Applied Physics Letters, **44** (7): 651, 1984.

[6] U. Dürig, D. W. Pohl and F. Rohner, Near-field optical-scanning microscopy, Journal of Applied Physics, **59**: 3318, 1986.

[7] M. J. Rust, M. Bates and X. Zhuang, Sub-diffraction-limit imaging by stochastic optical reconstruction microscopy (STORM), Nature Methods **3**: 793-796, 2006.

[8] E. Betzig, G. H. Patterson, R. Sougrat, O. W. Lindwasser, S. Olenych, J. S. Bonifacino, M. W. Davidson, J. Lipponcott-Schwartz and H. F. Hess, Imaging Intracellular Fluorescent Proteins at Nanometer Resolution, Science **313**(5793): 1642-1645, 2006.

[9] S. G. Lipson, H. Lipson and D. S. Tannhauser, Optical Physics, Third Edition, Cambridge University Press, 1995.

[10] B. G. Airy, On the Diffraction of an Object-glass with Circular Aperture, Transactions of the Cambridge Philosophical Society, **5** (1835): 283-291, 1835.

[11] B. Zhang, J. Zerubia, and J.-C. Olivo-Marin, Gaussian approximations of fluorescence microscope point-spread function models, Applied Optics **46** (10): 1819–1829, 2007.

[12] M. Göppert Mayer, Über Elementarakte mit zwei Quantensprüngen, Annals of Physics, **9** (3): 273-295, 1931.

[13] W. Kaiser and C. Garrett, Two-Photon Excitation in CaF_2:Eu^{2+}, Physical Review Letters, **7** (6): 229-231, 1961.

[14] E. H. Synge, A suggested method for extending microscopic resolution into the ultra-microscopic region, Philosophical Magazine, **6** (35): 356, 1928.

[15] M. Tsang, R. Nair, X.-M. Lu, Quantum theory of superresolution for two incoherent optical point sources, arXiv:1511.00552.

[16] A. van den Bos, Parameter Estimation for Scientists and Engineers, John Wiley & Sons, Hoboken, 2007

[17] C. W. Helstrom, Quantum Detection and Estimation Theory, Academic Press, New York, 1976.

[18] E. C. G. Sudarshan, Equivalence of Semiclassical and Quantum Mechanical Descriptions of Statistical Light Beams, Physical Review Letters, **10**: 277, 1963.

[19] L. Mandel and E. Wolf, Optical coherence and quantum optics, Cambridege University Press, 1995

[20] H. L. Van Trees, Detection, Estimation, and Modulation Theory, Part I. John Wiley & Sons, New York, 2001.

[21] M. J. Collett, R. Loudon and C. W. Gardiner, Quantum Theory of Optical Homodyne and Heterodyne Detection, journal of Modern Optics, **34** (6/7): 881, 1987.

[22] U. Leonhardt, Measuring the quantum state of light, Cambridge University Press, 1997.

[23] A. I. Lvovsky, H. Hansen, T. Aichele, O. Benson, J. Mlynek and S. Schiller, Quantum State Reconstruction of the Single-Photon Fock State, Physical Reivew Letters, **87**, 050402, 2001.

[24] P. Palittapongarnpim, A. MacRae and A. I. Lvovsky, Note: A Monolithic Filter Cavity for Experiments in Quantum Optics, Review of Scientific Instruments **83**, 066101, 2012.

[25] A. E. Siegman, Lasers, University Science Books, Mill Valley, 1986.

[26] Drever, R. W. P., Hall, J. L., Kowalski, F. V., Hough, J., Ford, G. M., Munley and A. J. H. Ward, Laser phase and frequency stabilization using an optical resonator, Applied Physics B **31** (2): 97–105, 1983.

[27] https://www.sparkfun.com/products/12779

[28] J. L. Devore, Probability and statistics for egineering and the sciences, Eight Edition, Cengage Learning, 2011.

[29] M. T. L. Hsu, V. Delaubert, P. K. Lam and W. P. Bowen, Optimal optical measurement of small displacements, Journal of Opitcs B: Quantum and semiclassical Optics **6**:496-501, 2004

[30] A. I. Lvovsky, M. G. Raymer, Continuous-variable optical quantum-state tomography, Reviews of Modern Physics, **81**: 299, 2009.

[31] R. Nair and M. Tsang, Interferometric superlocalization of two incoherent optical point sources, Optics Express **24** (4): 3584 (2016).

[32] T. Z. Sheng, K. Durak, A. Ling, Fault-tolerant and finite-error localization for point emitters within the diffraction limit, arXiv:1605.07297.

[33] W.-K. Tham, H. Ferretti, A. M. Steinberg, Beating Rayleigh's Curse by Imaging Using Phase Information, arXiv:1606.02666.

[34] M. Paur, B. Stoklasa, Z. Hradil, L. L. Sanchez-Soto and J. Rehacek, Achieving quantum-limited optical resolution, arXiv:1606.08332.